

A stable and accurate X-FFT solver for linear elastic homogenization problems in 3D

Flavia Gehrig¹ and Matti Schneider^{1,2,3,*}

¹University of Duisburg-Essen, Institute of Engineering Mathematics

²Fraunhofer Institute for Industrial Mathematics ITWM, Kaiserslautern

³Center for Nanointegration Duisburg-Essen (CENIDE)

*correspondence to: matti.schneider@uni-due.de

January 6, 2026

Abstract

Although FFT-based methods are renowned for their numerical efficiency and stability, traditional discretizations fail to capture material interfaces that are not aligned with the grid, resulting in sub-optimal accuracy. To address this issue, the work at hand introduces a novel FFT-based solver that achieves interface-conforming accuracy for three-dimensional mechanical problems. More precisely, we integrate the extended finite element (X-FEM) discretization into the FFT-based framework, leveraging its ability to resolve discontinuities via additional shape functions. We employ the modified abs(olute) enrichment and develop a preconditioner based on the concept of strongly stable GFEM, which mitigates the conditioning issues observed in traditional X-FEM implementations. Our computational studies demonstrate that the developed X-FFT solver achieves interface-conforming accuracy, numerical efficiency, and stability when solving three-dimensional linear elastic homogenization problems with smooth material interfaces.

Keywords: Computational homogenization; FFT-based computational micromechanics; Extended finite element method (X-FEM); Generalized finite element method (GFEM); Preconditioning; Iterative solver

1 Introduction

1.1 State of the art

To understand the behavior of complex materials, developing efficient and accurate simulation techniques turns out to be essential. Over the last decade, methods based on the fast Fourier transform (FFT) [1, 2] became increasingly popular due to their efficiency, which rests on:

- their low memory footprint due to their matrix-free formulation,
- their speed due to the use of state-of-the-art FFT implementations [3, 4] and dedicated iterative solution schemes,
- their use of regular grids, eliminating the need of expensive mesh generation and enabling to operate on μ -CT data [5] directly,
- their stability, which is rooted in their preconditioning strategy that leads to a mesh-independent upper bound on the condition number,
- their parallelizability.

For an overview of FFT-based methods, we refer to the review articles [6–9].

In the 1990s, Moulinec-Suquet [1, 2] introduced FFT-based methods by reformulating the cell problem as the Lippmann-Schwinger equation for elasticity [10, 11] and solving it using an FFT-based iterative method known as the basic scheme. Around 2014, the original method was decomposed into its constituent parts - discretization and solution scheme [12–15]. Moreover, the Fourier-based discretization of Moulinec-Suquet was interpreted as a trigonometric collocation discretization [16] and a nonconforming Fourier-Galerkin discretization [14], while the basic scheme was identified as a variant of the gradient descent method [17] and the Richardson iteration [18]. These insights enabled incorporating alternative discretizations and solvers into FFT-based methods. By adapting solution schemes from large scale optimization [19–21] the speed of FFT-based methods could be significantly improved. Moreover, discretizations based on voxel-wise constant fields [12, 22, 23], Fourier-Galerkin methods [24–26], finite volumes [27–29], finite differences [30–32] and finite elements (FEs) [33–35] were introduced in the context of FFT-based computational micromechanics.

For some discretizations, a superconvergence phenomenon was observed in FFT-based methods, where the effective stress converges at a quadratically higher rate than the local stress field [36]. For linear elasticity problems that are discretized by trilinear hexahedral FEs, Ye-Chung [37] first proved the superconvergence of FFT-based methods and derived explicit convergence rates. Subsequently, Schneider [38] proved that the convergence rates of the traditional Fourier-based discretization and the voxel finite element method (FEM) coincide. Put differently, for voxel finite element discretizations and the traditional Fourier-based discretization, the effective stress converges with the rate $\mathcal{O}(h)$ and the local stress/strain fields converge with the rate $\mathcal{O}(\sqrt{h})$ to the exact solution, where the mesh parameter h stands for the voxel edge length. These convergence rates are suboptimal compared to the quadratically higher rates of interface-conforming FEM with linear tetrahedral or bi-/trilinear hexahedral FEs [39, 40]. Essentially, the suboptimal convergence rates of the voxel finite element discretizations and the traditional Fourier-based discretization result because of the inaccurate approximation capabilities of voxels for general interfaces [41].

To achieve higher accuracy, composite voxels [42, 43] were introduced, which apply an averaging rule to the voxels that include an interface. Composite voxels with Voigt averaging [42–44] were found to lead to the most accurate results for composites with voids, whereas composite voxels with Reuss averaging [42, 43, 45, 46] are best suited for rigid inclusions. For finite material contrasts, composite voxels, which are furnished with the effective properties of an equivalent laminate [43, 47, 48] were found to yield the most accurate results. There are different ways to obtain the interface and subvolume fraction data

required for the laminate mixing rule: Either, microstructure images with a higher resolution may be used [49, 50] or a level-set description may be exploited [48]. Although improving the accuracy in linear elastic homogenization problems, the solution fields of the composite voxels still converge with the same rate as those of voxel FEM [48, Fig. 7B].

A different strategy to improve the accuracy of FFT-based methods was introduced by Zecevic et al. [51, 52]. Their local mesh morphing approach involves mapping from an interface-conforming grid to a reference configuration, applying the FFT-based method in the reference configuration, and mapping back to the interface-conforming grid. For simple microstructures, the interface-conforming grid and the mapping operator can be computed explicitly [51]. More complex microstructures can be treated using alternative methods, such as balancing a system of springs connecting the nodes [52] or employing grid adaptation based on optimal transport [53]. Nevertheless, generating the interface-conforming grid and mapping operator significantly increases the computational cost, and conditioning problems are expected for severely deformed grids.

Recently, a novel FFT-based framework [54] was introduced for two-dimensional thermal homogenization problems, which achieves interface-conforming accuracy while maintaining numerical efficiency and well-conditioning. This so-called X-FFT solver [54] integrates an extended finite element discretization with modified abs(olute) enrichment and a dedicated preconditioning strategy into FFT-based methods. The extended finite element method (X-FEM) resolves discontinuities in a regular grid setting by locally enriching the polynomial approximation space of the classical FE shape functions with additional shape functions that incorporate the discontinuity. Based on X-FEM, *weak* discontinuities, i.e., discontinuities in the gradient, as well as *strong* discontinuities, i.e., discontinuities in the primary solution field, may be modeled. Initially, X-FEM was developed to resolve crack paths without any re-meshing during crack evolution [55, 56]. However, its application was extended to fluid mechanics [57, 58], magnetic and coupled magneto-mechanical boundary value problems [59, 60], poromechanics [61] and contact mechanics [62]. In solid mechanics, X-FEM was used to model grain boundaries in polycrystals [63] (strong discontinuities) and material interfaces [64, 65] (weak discontinuities). The X-FEM is closely related to the generalized finite element method (GFEM) [66, 67]. Both methods use standard FE shape functions to realize the partition of unity (PU) [68]. Initially, the GFEM employed global enrichments, whereas the X-FEM performs local enrichments on a subset of nodes. However, the characteristics of GFEM evolved over time, shifting towards local enrichments. Due to this development, the terms X-FEM and GFEM are often used interchangeably [69, 70]. For a detailed history of the X-FEM and GFEM, we refer to section 1.1 of the review article by Fries and Belytschko [69]. For simplicity, we will use the term X-FEM to refer to both methods for the remainder of this manuscript.

To model smooth material interfaces in X-FEM, enrichment functions that rely on the level set method [71] are suitable, as the level set method offers an implicit description of a smooth interface. As a result, applications to micromechanics require microstructure generation methods that provide a level-set representation of the primitives of the microstructure. Fortunately, there are respective methods available for spherical [72, 73] and cylindrical inclusions [74, 75], irregular shaped particles [76–78], cellular materials [79] and woven composites [80]. A recently introduced approach encodes the level set information by a neural network in so-called Implicit Neural Representations (INRs) [81].

A suitable enrichment for modeling smooth material interfaces in X-FEM is the modified abs enrichment [65], which leverages the level set method and vanishes outside elements that comprise a material interface, thereby preventing parasitic terms in neighboring elements. The modified abs enrichment was shown to enable interface-conforming accuracy in X-FEM [65, 82], among other enrichments [57, 83]. Nevertheless, some formulations of the X-FEM suffer from ill-conditioned systems [69, 70].

To tackle the ill-conditioning, preconditioners based on Cholesky decompositions [84, 85], domain decom-

position strategies [85–87] and multigrid methods [88, 89] were developed. For two-dimensional thermal problems, Babuška et al. [70, 90] proved that, with a suitable enrichment and preconditioning strategy involving a diagonal preconditioner for the extended degrees of freedom, the condition number of the preconditioned X-FEM system matrix scales at the same rate as the underlying FEM system matrix with the mesh spacing h , namely, at the rate $\mathcal{O}(h^2)$. Moreover, they proved that for the so-called strongly stable X-FEM two mesh-independent bounds exist: one on the condition number of the preconditioned X-FEM system matrix and one on the condition number of the enriched block matrix [70]. The group showed that the X-FEM with the modified absolute enrichment and a suitable preconditioning strategy leads to a strongly stable X-FEM [70, 88] for two-dimensional thermal problems. The strongly stable X-FEM was extended to time-dependent problems, i.e., moving interfaces [91]. However, the authors of this manuscript are not aware of any extension of the strongly-stable X-FEM to three-dimensional thermal problems or to linear elasticity for material interface problems. To improve the numerical efficiency of X-FEM, dedicated iterative solvers were developed. On the one hand, multigrid solvers [87, 92] and multigrid preconditioned conjugate gradient solvers [88, 89] were tailored to X-FEM. On the other hand, FFT-based solvers were made available for X-FEM [54] in two-dimensional thermal problems based on the concept of strongly stable X-FEM [70].

1.2 Contributions

This work presents a novel X-FFT solver that solves three-dimensional mechanical problems with interface-conforming accuracy, overcoming a major limitation of classical FFT-based methods. Building on our recent work on X-FFT solvers for two-dimensional heat conductivity [54], we extend the approach to three-dimensional mechanical problems. However, the recently introduced X-FFT solver heavily relies on the proof for the existence of a mesh-independent upper bound on the condition number in a strongly stable X-FEM, provided by Babuška et al. [70], which is limited to two-dimensional heat conductivity problems. To date, we are not aware of such a proof for three-dimensional mechanical homogenization problems. Moreover, mechanical problems often involve complex material properties and operators without minor symmetries, which potentially worsens the conditioning and increases the implementation effort compared to heat conductivity problems. This work presents the modification of the recently introduced X-FFT solver [54] to address three-dimensional mechanical homogenization problems, discusses its implementation, and provides a comprehensive numerical analysis. Our primary research question is:

Does the displacement-based X-FFT solver extend to FFT-based computational homogenization methods in 3D mechanics with the expected accuracy and efficiency?

Efficiency relies on the existence of a mesh-independent upper bound on the condition number of the preconditioned system matrix, ensuring that the system remains stable even when the mesh spacing or position changes. Our studies indicate that such a mesh-independent bound holds for 3D mechanical homogenization with smooth interfaces. Moreover, we observe interface-conforming accuracy in the local and effective error convergence rates. Currently, the X-FFT solver applies to linear elastic, non-porous, multiphase materials with periodic boundary conditions and a single interface per element.

2 The X-FFT solver

2.1 Discretization by extended finite elements

We assume a three-dimensional cuboid cell

$$Y = [0, \ell_1] \times [0, \ell_2] \times [0, \ell_3] \quad (2.1)$$

with periodic boundary conditions, where a stress operator

$$\boldsymbol{\sigma} : Y \times \text{Sym}(3) \rightarrow \text{Sym}(3) \quad (2.2)$$

is defined that maps for every point $\mathbf{x} \in Y$ a strain tensor $\boldsymbol{\varepsilon} \in \text{Sym}(3)$ to a stress tensor $\boldsymbol{\sigma}(\mathbf{x}, \boldsymbol{\varepsilon})$. We aim to solve the weak form of the (quasi-) static equilibrium without microscopic body forces, so that the equation

$$\int_Y \boldsymbol{\nabla}^s \mathbf{v} : \boldsymbol{\sigma}(\mathbf{x}, \boldsymbol{\varepsilon}(\mathbf{x})) dV(\mathbf{x}) = 0 \quad (2.3)$$

holds for all test fields \mathbf{v} in the first-order Sobolev space $H_{\#}^1(Y; \mathbb{R}^3)$ of periodic fields with vanishing mean. The strain field

$$\boldsymbol{\varepsilon}(\mathbf{x}) = \bar{\boldsymbol{\varepsilon}} + \boldsymbol{\nabla}^s \mathbf{u}(\mathbf{x}) \quad (2.4)$$

consists of the average strain $\bar{\boldsymbol{\varepsilon}} \in \text{Sym}(3)$ and the symmetric gradient of the displacement fluctuation $\mathbf{u} \in H_{\#}^1(Y; \mathbb{R}^3)$. In the context of linear elasticity, the stress operator

$$\boldsymbol{\sigma}(\mathbf{x}, \boldsymbol{\varepsilon}) = \mathbb{C}(\mathbf{x}) : \boldsymbol{\varepsilon}(\mathbf{x}) \quad (2.5)$$

is defined by a linear mapping via the local stiffness tensor $\mathbb{C}(\mathbf{x}) \in \text{Lin}(\text{Sym}(3))$, which has minor and major symmetries. Moreover, we assume that the inequalities

$$C_- \|\boldsymbol{\varepsilon}\|^2 \leq \boldsymbol{\varepsilon} : \mathbb{C}(\mathbf{x}) : \boldsymbol{\varepsilon} \leq C_+ \|\boldsymbol{\varepsilon}\|^2 \quad \text{for all } \boldsymbol{\varepsilon} \in \text{Sym}(3) \quad (2.6)$$

hold at all points $\mathbf{x} \in Y$ for some positive constants $C_-, C_+ \in \mathbb{R}$. The bounds encode that the local stiffness tensor field is uniformly positive definite on the strains and uniformly bounded.

To discretize the weak form of the (quasi-) static equilibrium without microscopic body forces (2.3) by extended finite elements on a regular grid, we define a suitable X-FEM approximation space V_h . With this space at hand, we seek a displacement fluctuation field $\mathbf{u}_h \in V_h$ that satisfies the equation

$$\int_Y \boldsymbol{\nabla}^s \mathbf{v}_h : \mathbb{C} : (\bar{\boldsymbol{\varepsilon}} + \boldsymbol{\nabla}^s \mathbf{u}_h) d\mathbf{x} = 0 \quad (2.7)$$

for all test fields $\mathbf{v}_h \in V_h$. To develop a suitable X-FEM approximation space, we adapt the X-FEM approximation space for two-dimensional thermal problems [54, eq.(2.16)] to three-dimensional mechanical homogenization problems. The resulting X-FEM approximation space takes the form

$$V_h = \left\{ \sum_{i \in I} N_{\text{FE}}^i \mathbf{u}_{\text{FE}}^i + \sum_{j \in J} N_{\text{X}}^j \mathbf{u}_{\text{X}}^j \mid i \in I, \quad j \in J, \quad \mathbf{u}_{\text{FE}}^i \in \mathbb{R}^3, \quad \mathbf{u}_{\text{X}}^j \in \mathbb{R}^3, \quad \sum_{i \in I} \mathbf{u}_{\text{FE}}^i = \mathbf{0} \right\} \quad (2.8)$$

with the nodes i , which are in the set of standard FE nodes I , and the enriched nodes j , which are in the set of enriched nodes J . The set of enriched nodes J is a subset of the set of standard FE nodes I . Typically, the latter set has a much higher cardinality. Moreover, the X-FEM approximation space for three-dimensional mechanical problems (2.8) consists of the standard nodal FE shape functions N_{FE}^i , the standard nodal displacement fluctuations \mathbf{u}_{FE}^i , the enriched nodal FE shape functions N_{X}^j , and the

enriched nodal displacement fluctuations \mathbf{u}_X^j . The standard FE displacement fluctuations are forced to be mean free, so that eq.(2.7) admits a unique solution. The enriched shape functions take the form

$$N_X^j(\mathbf{x}) = N_{\text{FE}}^j(\mathbf{x}) \rho(\mathbf{x}), \quad \mathbf{x} \in Y, \quad (2.9)$$

where the scalar-valued function ρ stands for the enrichment function. For matrix-inclusion composites, we seek to approximate the kink in the displacement fluctuation at the interface by the enrichment function ρ . To approximate these so-called *weak discontinuities*, enrichment functions based on the level set description [71] of the interface may be used [64, 65]. A level set function $L : Y \rightarrow \mathbb{R}$ provides an implicit description of a composite comprising two phases Y_{\pm} with interface I based on the definitions

$$I = \{\mathbf{x} \in Y \mid L(\mathbf{x}) = 0\}, \quad (2.10)$$

$$Y_+ = \{\mathbf{x} \in Y \mid L(\mathbf{x}) > 0\}, \quad (2.11)$$

$$Y_- = \{\mathbf{x} \in Y \mid L(\mathbf{x}) < 0\}, \quad (2.12)$$

where the level set function is assumed to be smooth and at least Lipschitz continuous [71]. For numerical reasons, it is convenient to normalize the level set function, such that its values encode the signed distance to the closest interface [48]. If the nodal level set values L^i are available, i.e., via an analytical description of the interface, the continuous level set function may be approximated by linear interpolation via the FE shape functions in the form

$$L_h(\mathbf{x}) = \sum_{i \in I} N_{\text{FE}}^i(\mathbf{x}) L^i. \quad (2.13)$$

For an example of an interface with respective level set function, we refer to Fig. 1(a) and Fig. 1(b). Sukumar et al. [64] pioneered using level set based enrichments for interface problems by introducing the *abs enrichment*

$$\rho^a(\mathbf{x}) = \left| \sum_{i \in I} N_{\text{FE}}^i(\mathbf{x}) L^i \right|. \quad (2.14)$$

However, the *abs enrichment* (2.14) leads to poor conditioning due to linear dependencies between the FE and the enriched shape functions. As a remedy, Moës et al. [65] introduced the *modified abs enrichment*, which takes the form

$$\rho^m(\mathbf{x}) = \sum_{i \in I} N_{\text{FE}}^i(\mathbf{x}) |L^i| - \left| \sum_{i \in I} N_{\text{FE}}^i(\mathbf{x}) L^i \right|, \quad \mathbf{x} \in Y. \quad (2.15)$$

The *modified abs enrichment* (2.15) is constructed by subtracting the *abs enrichment* (2.14) from its linear interpolant. By construction, the *modified abs enrichment* (2.15) vanishes in all elements that do not contain an interface, so that linear dependencies between the FE and enriched shape functions are prevented. For a visualization of the *modified abs enrichment* of the interface shown in Fig. 1(a), we refer to Fig. 1(c).

2.2 Preconditioning with internal scaling

In the previous subsection, we discretized the weak form of the (quasi-) static equilibrium without microscopic body forces by extended finite elements on a regular grid for linear elasticity. To decrease the effort required to solve the resulting system (2.7), we introduce a preconditioning strategy based on concepts that were recently developed for two-dimensional thermal problems [54, 70, 93].

Traditionally, the condition number of X-FEM systems scales with the rate $\mathcal{O}(h^{-4})$ in the mesh spacing h [90]. Babuška et al. [70, 90] proved that for some conditions on the enrichment space and for two-dimensional thermal problems, the condition number of the X-FEM system reduces to the rate of an

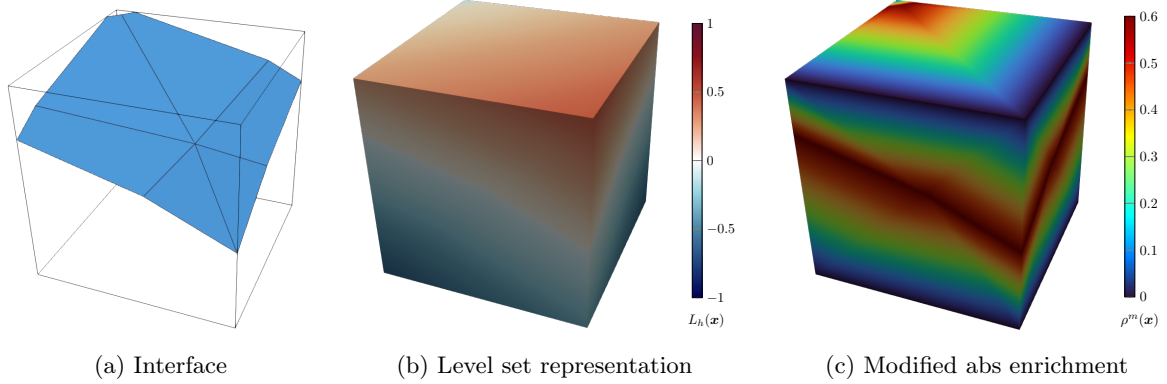


Figure 1: Interface with level set representation and modified abs enrichment function of a voxel that is discretized by six \mathbb{P}_1 elements.

underlying voxel-FEM system, namely the rate $\mathcal{O}(h^{-2})$. Moreover, in their so-called strongly stable X-FEM [70], applying a diagonal preconditioner to the enriched degrees of freedom guarantees mesh-independent upper bounds on the condition numbers of the preconditioned X-FEM system and the preconditioned system of the enriched degrees of freedom. Based on the inequalities that Babuška et al. [70] use to derive these mesh-independent upper bounds, the authors of this manuscript developed an X-FFT preconditioner [54, Sec.3] for two-dimensional thermal problems that leads to a mesh-independent upper bound on the condition number of the preconditioned X-FFT system. In a subsequent publication, the authors [93] introduced an internal scaling of the enriched shape functions to prevent numerical instabilities that could arise if the enriched shape functions and the standard FE shape functions have different order of magnitude. To construct a preconditioner for the work at hand, we transfer the strategies that were previously developed for 2D thermal homogenization problems [54, 93] to three-dimensional linear elastic unit-cell problems. However, we note that a proof extending Babuška et al. [70, §5] to three-dimensional mechanics is currently not known to the authors. Rather, we report computational experiments, see section 4.

Building on the previously developed internal scaling strategy [93], we introduce the scaled enriched shape function

$$\tilde{N}_X^j = (\underline{\underline{D}}_{jj}^0)^{-\frac{1}{2}} N_X^j \quad (2.16)$$

and the scaled enriched displacement fluctuation

$$\tilde{u}_X^j = (\underline{\underline{D}}_{jj}^0)^{\frac{1}{2}} u_X^j \quad (2.17)$$

with the scaling factors

$$(\underline{\underline{D}}_{jj}^0)_{jj} = \int_Y \|\nabla^s N_X^j\|^2 dx \quad (2.18)$$

that are based on the formerly introduced diagonal preconditioner [54, eq.(3.10)]. These scaled enriched shape functions are designed to improve the numerical stability by preventing the enriched shape functions from having a different order of magnitude than the standard FE functions. More precisely, for the standard FE functions at the node $k \in I$, by definition, the interpolation condition

$$N_{FE}^k(x_p) = \delta_{kp} \quad (2.19)$$

holds at the node $p \in I$. To obtain values in the same order of magnitude for the scaled enriched shape functions, we require the condition

$$\|\nabla^s \tilde{N}_X^j\|_{L^2} = 1, \quad (2.20)$$

to hold at all enriched nodes $j \in J$, which is fulfilled by the scaled enriched shape function (2.16) defined above. We note that we rely on the symmetrized gradient ∇^s in the definition of the scaling factors (2.18) for three-dimensional linear elasticity, a choice that is motivated by the kinematic compatibility condition. The adapted X-FFT approximation space (2.8) takes the form

$$\tilde{V}_h = \left\{ \sum_{i \in I} N_{\text{FE}}^i \mathbf{u}_{\text{FE}}^i + \sum_{j \in J} \tilde{N}_{\text{X}}^j \tilde{\mathbf{u}}_{\text{X}}^j \mid i \in I, \quad j \in J, \quad \mathbf{u}_{\text{FE}}^i \in \mathbb{R}^3, \quad \tilde{\mathbf{u}}_{\text{X}}^j \in \mathbb{R}^3, \quad \sum_{i \in I} \mathbf{u}_{\text{FE}}^i = \mathbf{0} \right\}. \quad (2.21)$$

After selecting a basis of the adapted X-FEM approximation space (2.21), we may rewrite the discretized weak form of the (quasi-) static equilibrium (2.7) as the linear system

$$\underline{\underline{\tilde{A}}} \underline{\tilde{u}} = \underline{b} \quad (2.22)$$

with the scaled system matrix

$$\underline{\underline{\tilde{A}}} = \begin{bmatrix} \underline{\underline{A}}_{11} & \underline{\underline{A}}_{12} \\ \underline{\underline{A}}_{21} & \underline{\underline{A}}_{22} \end{bmatrix} \in \mathbb{R}^{3(n_{\text{FE}}+n_{\text{X}}) \times 3(n_{\text{FE}}+n_{\text{X}})}, \quad (2.23)$$

the scaled solution vector

$$\underline{\tilde{u}} = \begin{pmatrix} \underline{u}_1 \\ \underline{\tilde{u}}_2 \end{pmatrix} \in \mathbb{R}^{3(n_{\text{FE}}+n_{\text{X}})} \quad (2.24)$$

and the scaled right-hand side vector

$$\underline{\tilde{b}} = \begin{pmatrix} \underline{b}_1 \\ \underline{\tilde{b}}_2 \end{pmatrix} \in \mathbb{R}^{3(n_{\text{FE}}+n_{\text{X}})}. \quad (2.25)$$

The number n_{FE} denotes the number of nodes and the number n_{X} accounts for the number of enriched nodes, i.e., the nodes of elements that contain an interface.

The upper left block matrix

$$\left(\underline{\underline{\tilde{A}}}_{11} \right)_{ij} = \int_Y \nabla^s N_{\text{FE}}^i : \mathbb{C} : \nabla^s N_{\text{FE}}^j d\mathbf{x}, \quad i, j = 1, 2, \dots, n_{\text{FE}}, \quad (2.26)$$

and the upper vector $\underline{u}_1 \in \mathbb{R}^{3n_{\text{FE}}}$ comprise solely classical FE degrees of freedom and are independent of the internal scaling. The lower right block matrix

$$\left(\underline{\underline{\tilde{A}}}_{22} \right)_{ij} = \int_Y \nabla^s \tilde{N}_{\text{X}}^i : \mathbb{C} : \nabla^s \tilde{N}_{\text{X}}^j d\mathbf{x}, \quad i, j = 1, 2, \dots, n_{\text{X}} \quad (2.27)$$

and the lower vector $\underline{u}_2 \in \mathbb{R}^{3n_{\text{X}}}$ depend solely on the enriched degrees of freedom, whereas the off-diagonal matrices

$$\left(\underline{\underline{\tilde{A}}}_{12} \right)_{ij} = \int_Y \nabla^s N_{\text{FE}}^i : \mathbb{C} : \nabla^s \tilde{N}_{\text{X}}^j d\mathbf{x}, \quad i = 1, 2, \dots, n_{\text{FE}}, \quad j = 1, 2, \dots, n_{\text{X}}, \quad (2.28)$$

$$\left(\underline{\underline{\tilde{A}}}_{21} \right)_{ij} = \int_Y \nabla^s \tilde{N}_{\text{X}}^i : \mathbb{C} : \nabla^s N_{\text{FE}}^j d\mathbf{x}, \quad i = 1, 2, \dots, n_{\text{X}}, \quad j = 1, 2, \dots, n_{\text{FE}}, \quad (2.29)$$

quantify the interaction between the classical FE and the enriched degrees of freedom. To precondition the linear system (2.22), we rely on the X-FFT preconditioner [93] that was originally developed for two-dimensional thermal problems and takes the form

$$\underline{\underline{\tilde{P}}} = \begin{bmatrix} \underline{\underline{A}}_{11}^0 & \underline{\underline{I}} \\ \underline{\underline{I}} & \underline{\underline{I}} \end{bmatrix} \in \mathbb{R}^{3(n_{\text{FE}}+n_{\text{X}}) \times 3(n_{\text{FE}}+n_{\text{X}})} \quad (2.30)$$

for three-dimensional mechanical problems. The X-FFT solver (2.30) consists of the the identity matrix $\underline{\underline{I}} \in \mathbb{R}^{3n_{\text{FE}} \times 3n_{\text{FE}}}$ and the constant coefficient preconditioner

$$\left(\underline{\underline{A}}_{11}^0\right)_{ij} = \int_Y \nabla^s N_{\text{FE}}^i : \nabla^s N_{\text{FE}}^j d\mathbf{x}, \quad i, j = 1, 2, \dots, 3n_{\text{FE}}, \quad (2.31)$$

which uses the symmetrized gradient ∇^s in consistency with the scaling factors (2.18). Applying the block preconditioner (2.30), the linear system (2.22) takes the form

$$\underline{\underline{A}}_{11}^0^{-1} \left(\underline{\underline{A}}_{11} \underline{u}_1 \right) + \underline{\underline{A}}_{22} \underline{\tilde{u}}_2 = \underline{\underline{P}}^{-1} \underline{b}. \quad (2.32)$$

For voxel-based FEs, the constant coefficient preconditioner (2.31) may be inverted efficiently via the fast Fourier transform such that Green's operator results. In practice, we use well-established strategies from the literature [33–35] to compute the preconditioner and cache it. We refer to Schneider [94] for a summary of the used strategies.

3 Implementation

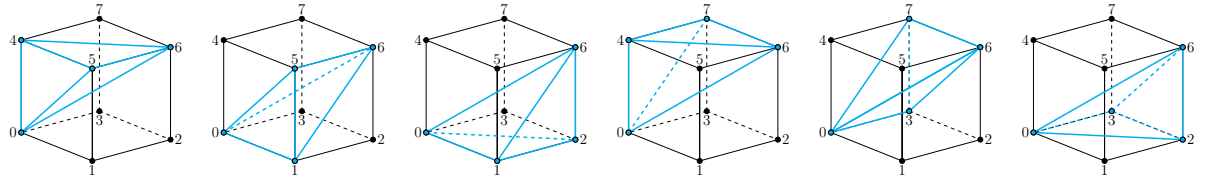


Figure 2: Division of the voxel into six \mathbb{P}_1 elements [95].

Our X-FFT solver applies an iterative scheme to solve the linear system (2.22) utilizing the preconditioner (2.30). For efficient implementation it is convenient to treat the global linear system

$$\underline{\underline{\tilde{A}}} \underline{\tilde{u}} - \underline{b} = 0 \quad (3.1)$$

with a divide-and-conquer strategy on the element level, such that the form

$$\sum_{e=1}^{n_e} \underline{\underline{\Lambda}}_e^T \left(\underline{\underline{\tilde{A}}}_e \underline{\tilde{u}}_e - \underline{b}_e \right) = 0 \quad (3.2)$$

results, where the matrix $\underline{\underline{\Lambda}}_e \in \mathbb{R}^{3(n_{\text{FE}}+n_{\text{N}}) \times n_{\text{N}}}$ associates the global degrees of freedom with the element nodal degrees of freedom n_{N} . We assume that each voxel consists of six \mathbb{P}_1 elements as depicted in Fig. 2. Via the utilized X-FFT approximation space (2.21) nodes that are not located on elements containing an interface, i.e., nodes $k \in I \setminus J$, have solely three standard FE degrees of freedom per node ($n_{\text{N}} = 3$). In contrast, nodes that belong to enriched elements, i.e., nodes $k \in J$, have six degrees of freedom per node ($n_{\text{N}} = 6$). The relations

$$\underline{\tilde{u}}_e = \underline{\underline{\Lambda}}_e \underline{\tilde{u}}, \quad (3.3)$$

$$\underline{\underline{A}}_e = \int_{Y_e} \nabla^s N_e(\mathbf{x})^T \underline{\underline{C}}(\mathbf{x}) \nabla^s N_e(\mathbf{x}) d\mathbf{x}, \quad (3.4)$$

$$\underline{b}_e = \int_{Y_e} \nabla^s N_e(\mathbf{x})^T \underline{\underline{C}}(\mathbf{x}) \bar{\boldsymbol{\varepsilon}} d\mathbf{x}, \quad (3.5)$$

hold with the symmetrized gradient of the nodal shape function $\nabla^s N_e(\mathbf{x}) \in \mathbb{R}^{6 \times 4n_{\text{N}}}$ and the local stiffness matrix $\underline{\underline{C}}$. Note that our implementation relies on the Voigt-Mandel notation for all matrices. At a point

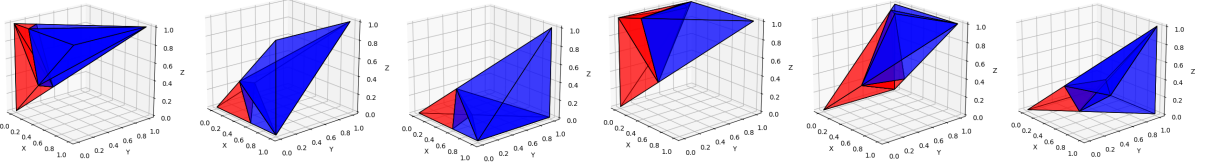


Figure 3: Division of the \mathbb{P}_1 elements into subtetrahedra for integration.

$\mathbf{x} \in Y$, the gradient of the nodal shape function may be computed using the scalar gradient of the nodal shape function via the relation

$$\underline{\underline{\underline{N}}}_e^{\text{scalar}}(\mathbf{x}) = \underline{\underline{M}} \underline{\underline{\nabla N}}_e^{\text{scalar}}(\mathbf{x}) \otimes \underline{\underline{I}}_{3 \times 3} \quad (3.6)$$

with the identity matrix $\underline{\underline{I}}_{3 \times 3}$ and the dyadic product \otimes . The matrix $\underline{\underline{M}}$ extracts the symmetrized (strain) part in Voigt-Mandel notation from a full deformation gradient. For a reference tetrahedron with nodes $ABCD$, the scalar gradient of the nodal shape function takes the form

$$\underline{\underline{\underline{N}}}_e^{\text{scalar}}(\mathbf{x}) = \begin{pmatrix} N_{\text{FE}}^A(\mathbf{x}) & N_{\text{FE}}^B(\mathbf{x}) & N_{\text{FE}}^C(\mathbf{x}) & N_{\text{FE}}^D(\mathbf{x}) & \tilde{N}_X^A(\mathbf{x}) & \tilde{N}_X^B(\mathbf{x}) & \tilde{N}_X^C(\mathbf{x}) & \tilde{N}_X^D(\mathbf{x}) \end{pmatrix} \quad (3.7)$$

for enriched elements and reduces to the first four entries for non-enriched elements. Using the modified abs enrichment (2.15), and the internal scaling factors (2.18), the representation

$$\tilde{N}_X^j(\mathbf{x}) = (\underline{\underline{D}}_j^0)^{-\frac{1}{2}} \rho^m(\mathbf{x}) N_{\text{FE}}^j(\mathbf{x}) \quad (3.8)$$

follows for the scaled enriched shape functions. For linear FE shape functions N_{FE}^j , the modified abs enrichment ρ^m (2.15) is piecewise linear, such that the enriched shape function \tilde{N}_X^j is quadratic in space. For enriched elements, the shape function gradient (3.6) is thus linear in space.

We aim to compute the integrals of the element stiffness matrix (3.4) and the element vector (3.5) via quadrature. The modified abs enrichment leads to a jump in the shape function gradient at the interface so that a non-continuous integrand results. However, when dividing the \mathbb{P}_1 into subtetrahedra [55,64] that resolve the linearized interface, exact integration via quadrature is possible. Schweiger and Arridgde [96, Fig. 2] provide an overview of the different subdivisions resulting from a tetrahedron cut by a single plane. For a specific example of such a subdivision, we refer to Fig. 3, where the colors blue and red denote the two different phases. For each subtetrahedron, we compute the quadrature points and weights according to Shunn and Ham [97, Appendix F]. Each voxel consists of six \mathbb{P}_1 elements and the maximum number of subtetrahedra per \mathbb{P}_1 element is six [96, Fig. 2]. As the integrand of the element stiffness matrix (3.4) is quadratic, four quadrature points per subtetrahedron are required [97, Appendix F]. Therefore, a maximum of 144 quadrature points per voxel are needed. With the quadrature points \mathbf{q}_α and the weights w_α at hand, the element stiffness matrix (3.4) and the element vector (3.5) take the form

$$\underline{\underline{\underline{A}}}_e^{\text{appr}} = \sum_{\alpha=1}^{q_e} w_\alpha \underline{\underline{\nabla N}}_e(\mathbf{q}_\alpha)^\top \underline{\underline{C}}(\mathbf{q}_\alpha) \underline{\underline{\nabla N}}_e(\mathbf{q}_\alpha), \quad (3.9)$$

$$\underline{\underline{\underline{b}}}_e^{\text{appr}} = \sum_{\alpha=1}^{q_e} w_\alpha \underline{\underline{\nabla N}}_e(\mathbf{q}_\alpha)^\top \underline{\underline{C}}(\mathbf{q}_\alpha) \bar{\underline{\underline{\epsilon}}}, \quad (3.10)$$

where the number q_e denotes the number of required quadrature points per element. The average stress per element may be computed by the equation

$$\langle \underline{\sigma}(\tilde{\mathbf{u}}_e) \rangle_{Y_e} = \underline{\underline{\underline{S}}}_e^{\text{appr}} \tilde{\mathbf{u}}_e \quad (3.11)$$

with the matrix

$$\underline{\underline{S}_e}^{\text{appr}} = \sum_{i=\alpha}^{q_e} w_i \underline{\underline{C}}(\mathbf{q}_\alpha) \underline{\underline{\nabla N}_e}(\mathbf{q}_\alpha) \quad (3.12)$$

that results from the quadrature scheme used. With these quantities at hand, we may compute the left-hand side of the linear system (3.2) at each iteration by the residual vector

$$\underline{r}(\tilde{\underline{u}}) = \sum_{e=1}^{n_e} \underline{\underline{\Lambda}_e}^T \left(\underline{\underline{\tilde{A}_e}}^{\text{appr}} \tilde{\underline{u}_e} - \underline{\underline{b}_e}^{\text{appr}} \right). \quad (3.13)$$

Following Schneider et al. [94], our implementation relies on the stopping criterion

$$\text{res}_k \stackrel{!}{\leq} \text{tol} \|\langle \underline{\underline{\sigma}}(\tilde{\underline{u}}^k) \rangle_Y\| \quad (3.14)$$

with the residual

$$\text{res}_k = \sqrt{\underline{r}(\tilde{\underline{u}}^k)^T \left(\underline{\underline{\tilde{P}}} \right)^{-1} \underline{r}(\tilde{\underline{u}}^k)}, \quad (3.15)$$

the desired tolerance tol, and the average stress

$$\langle \underline{\underline{\sigma}}(\tilde{\underline{u}}) \rangle_Y = \sum_{e=1}^{n_e} \langle \underline{\underline{\sigma}}(\tilde{\underline{u}}_e) \rangle_{Y_e}. \quad (3.16)$$

The residual (3.15) is computed using the scaled X-FFT preconditioner (2.30) that was derived in the previous section.

Algorithm 1 Displacement-based linear CG scheme for the X-FFT

Precompute and cache $\underline{\underline{A}_e}^{\text{appr}}$ and $\underline{\underline{S}_e}^{\text{appr}}$ per element

```

1:  $\tilde{\underline{u}} \leftarrow \underline{0}$ 
2:  $\underline{f} \leftarrow \underline{r}(\tilde{\underline{u}})$ 
3:  $\begin{bmatrix} \underline{d} \\ \text{res} \end{bmatrix} \leftarrow \begin{bmatrix} \underline{\underline{\tilde{P}}} \underline{f} \\ \sqrt{\underline{f}^T \underline{\underline{\tilde{P}}} \underline{f}} \end{bmatrix}$ 
4:  $\text{res}_{\text{old}} \leftarrow \text{res}$ 
5:  $k \leftarrow 1$ 
6: while  $k < \text{maxit}$  and  $\text{res} > \text{tol}$  do
7:    $k \leftarrow k + 1$ 
8:    $\underline{z} \leftarrow \underline{r}(\underline{d})$ 
9:    $\alpha \leftarrow \text{res}_{\text{old}}^2 / \langle \underline{z}, \underline{d} \rangle_{L_2}$ 
10:   $\begin{bmatrix} \tilde{\underline{u}} \\ \underline{f} \end{bmatrix} \leftarrow \begin{bmatrix} \tilde{\underline{u}} + \alpha \underline{d} \\ \underline{f} - \alpha \underline{z} \end{bmatrix}$ 
11:   $\begin{bmatrix} \underline{z} \\ \text{res} \end{bmatrix} \leftarrow \begin{bmatrix} \underline{\underline{\tilde{P}}} \underline{f} \\ \sqrt{\underline{f}^T \underline{\underline{\tilde{P}}} \underline{f}} \end{bmatrix}$ 
12:   $\beta \leftarrow \text{res}^2 / \text{res}_{\text{old}}^2$ 
13:   $\underline{d} \leftarrow \underline{z} + \beta \underline{d}$ 
14:   $\text{res}_{\text{old}} \leftarrow \text{res}$ 
15: end while

```

We may solve the X-FFT system (3.2) using the basic scheme [1, 2], the Barzilai Borwein scheme [20], the linear conjugate gradient scheme [19] or the nonlinear conjugate gradient scheme [98], among others [8, Tab.4]. The basic scheme [1, 2], renowned for its robustness and reliability, is interpretable as a gradient

descent method [17] or a Richardson iteration [18]. With the residual (3.15), the basic scheme may be implemented on two displacement fields. Nevertheless, the basic scheme only converges slowly to the solution of the Lippmann–Schwinger equation, with an iteration count that increases at a rate of order $O(\kappa)$ as the material contrast κ increases. The Barzilai Borwein scheme [20] accelerates the basic scheme with an advanced step size selection strategy, without requiring any additional memory footprint. The linear conjugate gradient (linear CG) method [19] is particularly well-suited for solving linear systems. Compared to the basic scheme, it does not require any internal parameters and improves the rate of the iteration count until convergence towards the rate $\mathcal{O}(\sqrt{\kappa})$ [8]. However, the implementation of linear CG requires four displacement fields, resulting in an increased memory footprint. The nonlinear conjugate gradient (nonlinear CG) method [98] is a generalization of linear CG towards unconstrained nonlinear optimization problems and operates on three displacement fields. While it offers a general-purpose solver for FFT-based computational micromechanics, its iteration count until convergence may be up to twice as high as that of linear CG in the special case of linear elasticity [98].

The nonlinear CG [98] and the Barzilai Borwein [20] scheme rely on the step size of the basic scheme. As the basic scheme is a Richardson iteration [18], the optimal step size may be computed based on the maximum and minimum eigenvalue of the system matrix. To compute the optimal step size for the X-FFT system at hand, the maximum and minimum eigenvalue of the preconditioned X-FFT system matrix would be required. However, computing these eigenvalues by assembling the preconditioned X-FFT system matrix would destroy the efficiency of the solver. As a band-aid solution, we choose the step size

$$s_0 = \frac{C_- + C_+}{2}, \quad (3.17)$$

where the parameter C_- (C_+) denotes the smallest (largest) stiffness eigenvalue of all individual materials comprising the matrix-inclusion problem. We acknowledge that the step size (3.17) is not optimal. However, since our X-FFT system (3.2) is currently limited to linear elasticity, the most suitable choice for solving the system is the linear CG scheme, which does not rely on the step size. Algorithm 1 outlines a displacement-based linear CG scheme that is adapted to our X-FFT solver. The other mentioned solution schemes may be used analogously. For all solution schemes used in this work, we precompute and cache the element stiffness matrix (3.9) and the average stress matrix (3.12), such that quadrature has to be computed only once per simulation instead of once per iteration. This caching strategy reduces the computational time associated with the high number of quadrature points required for subdivision integration, but at the cost of an increased memory footprint. For the implementation, we use Python with Cython extensions and leverage OpenMP parallelization to take advantage of multi-core processors.

4 Computational investigations

4.1 Setup

Our computational investigations comprise matrix inclusion problems with smooth and non-smooth interfaces. To validate the results of the X-FFT solver, we compare them to the results of other FE discretizations in FFT-based homogenization. The respective discretizations are listed in Tab. 1. We note that the rotated staggered grid discretization [30] may be interpreted as a voxel-segmented trilinear hexahedral Galerkin-FEM discretization with reduced integration [33]. For the composite voxels in the CoVo discretization, we use the level set-based strategy of Lendvai and Schneider [48] to compute the interface normals and volume fractions. In the CoVo discretization, the interface in each voxel is approximated by a single plane. Therefore, we correct the level set values using regression [48, Sec. 3.2] to obtain the best-fitting linear level-set function.

Shortcut	Discretization of homogeneous voxels	Discretization of interface voxels
P1	voxel-segmented Galerkin-FEM with \mathbb{P}_1 elements	-
Q1R	rotated staggered grid discretization [30]	-
CoVo	rotated staggered grid discretization [30]	composite voxel with laminate mixing rule [48, 49, 99]
X-FEM	voxel-segmented Galerkin-FEM with \mathbb{P}_1 elements	X-FEM (2.21)

Table 1: Discretizations.

We quantify the error of a scalar $a \in \mathbb{R}_{>0}$ w.r.t a reference value $a_{\text{ref}} \in \mathbb{R}$ by the relative error

$$e(a, a_{\text{ref}}) = \left| \frac{a - a_{\text{ref}}}{a_{\text{ref}}} \right|. \quad (4.1)$$

The L^2 -norm of a FE discretized vector field \mathbf{a} is evaluated by quadrature and takes the form

$$\|\mathbf{a}\|_{L^2} = \sqrt{\sum_{\alpha=1}^{n_{\text{int}}} w_{\alpha} \mathbf{a}(\mathbf{q}_{\alpha}) \cdot \mathbf{a}(\mathbf{q}_{\alpha})}, \quad (4.2)$$

where the parameters w_{α} and \mathbf{q}_{α} denote the respective quadrature weights and quadrature points.

For a conforming Galerkin method, we note that based on eq. (2.6) the error between the simulated and exact effective elastic energy, may be bounded from above by a value which is proportional to the quadratic error of the simulated local strain field $\boldsymbol{\varepsilon}_h$ to the exact solution $\boldsymbol{\varepsilon}_*$ via the relation

$$\bar{\boldsymbol{\varepsilon}} : (\mathbb{C}_*^{\text{eff}} - \mathbb{C}_h^{\text{eff}}) : \bar{\boldsymbol{\varepsilon}} \leq C_+ \|\boldsymbol{\varepsilon}_* - \boldsymbol{\varepsilon}_h\|_{L^2}^2 \quad (4.3)$$

with the simulated effective stiffness $\mathbb{C}_h^{\text{eff}}$ and the exact effective stiffness $\mathbb{C}_*^{\text{eff}}$. Moreover, the error in the local strain fields is bounded from above by a value proportional to the square root of the error in the effective elastic energy via the relation

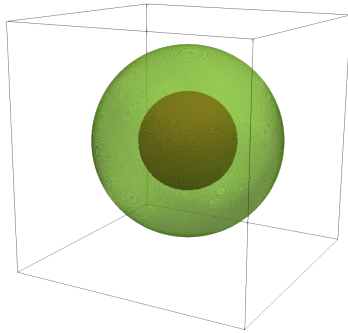
$$\|\boldsymbol{\varepsilon}_* - \boldsymbol{\varepsilon}_h\|_{L^2} \leq \sqrt{\frac{\bar{\boldsymbol{\varepsilon}} : (\mathbb{C}_*^{\text{eff}} - \mathbb{C}_h^{\text{eff}}) : \bar{\boldsymbol{\varepsilon}}}{C_-}}. \quad (4.4)$$

The positive constants $C_-, C_+ \in \mathbb{R}$ appearing in the inequalities above refer to the bounds on the stiffness (2.6). The derivation of the inequalities is discussed in Appendix A, based on previous work of Schneider [100]. We observe that, based on the inequalities (4.3) and (4.4), the error in the effective elastic energy is proportional to the squared error of the local strain fields for conforming Galerkin methods. Consequently, the error in the effective stress is proportional to the squared error of the local stress fields for these methods. Among the discretizations listed in Tab. 1, the X-FEM discretization and the P1 discretization are conforming Galerkin methods, so that the inequalities (4.3) and (4.4) hold respectively. All studies below were computed on a workstation with 1.15 TB RAM and 96 cores (2.4GHz).

4.2 Hashin's neutral inclusion

Microstructure

Our first study is dedicated to Hashin's neutral inclusion problem. Due to its analytical solution [101] that is available for the setup described below, we may assess the quality of the X-FFT solutions. We



(a) Geometry

	Matrix	Coating	Inclusion
Young's modulus in MPa	1.500000	1.212036	12.120361
Poisson's ratio	0.25	0.25	0.25
Radius in μm	-	2π	$6/5e$

(b) Parameters

Figure 4: Geometry and parameters of Hashin's neutral inclusion problem (e refers to Euler's number).

consider a cuboid cell with an edge length of $16\mu\text{m}$ that contains a coated sphere, which is embedded in a matrix phase, as shown in Fig. 4(a). All three phases are assumed to be isotropic, and a macroscopic uniform compression with loading $\bar{\varepsilon} = \mathbf{I}$ is prescribed. We resolve the cell by $16, 32, \dots, 1024$ voxels per dimension, denoted by the voxel count N per axis, which is the inverse of the mesh parameter h . Using the convergence criterion (3.14), the computations in this subsection were solved up to the tolerance $\text{tol} = 10^{-7}$. The utilized radii and material parameters are given in Tab. 4(b) - rounded to six digits for clarity. To allow for an analytical solution, the material parameters are chosen such that the analytical solution of the effective bulk modulus coincides with the matrix bulk modulus. For the respective equation on the effective bulk modulus and the analytical solution of the local displacement field, we refer to Schneider et al. [102, Sec. 4.1.1].

Solution scheme

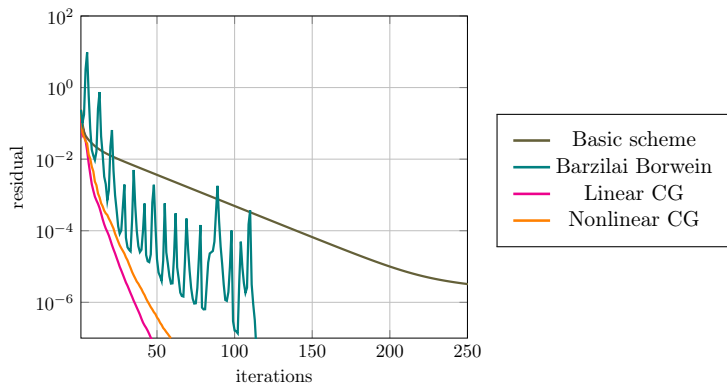


Figure 5: Solver convergence for X-FEM at voxel count $N = 128$ in Hashin's neutral inclusion.

For X-FEM at voxel count $N = 128$, we compare the convergence of linear CG [19] to other solvers, namely to the basic scheme [1, 2], the Barzilai Borwein scheme [20] and the nonlinear CG scheme [98]. The respective convergence of the residual (3.15) with the iteration count of the different solvers is shown in Fig. 5. We observe that the residual of the basic scheme converges monotonically but slowly with increasing iteration count, reaching the desired tolerance at iteration count 668. However, the convergence rate is anticipated to worsen with increasing material contrast. In contrast, the residual of

the Barzilai Borwein scheme does not converge monotonically with increasing iteration count, but reaches the desired tolerance 10^{-7} at iteration count 115. The nonlinear CG scheme requires 60 iterations to reach the desired tolerance, while linear CG achieves this in only 48 iterations. This decreased iteration count of linear CG in linear elasticity is well-documented in the literature [98]. Therefore, we choose to use linear CG for the remainder of this section.

Accuracy

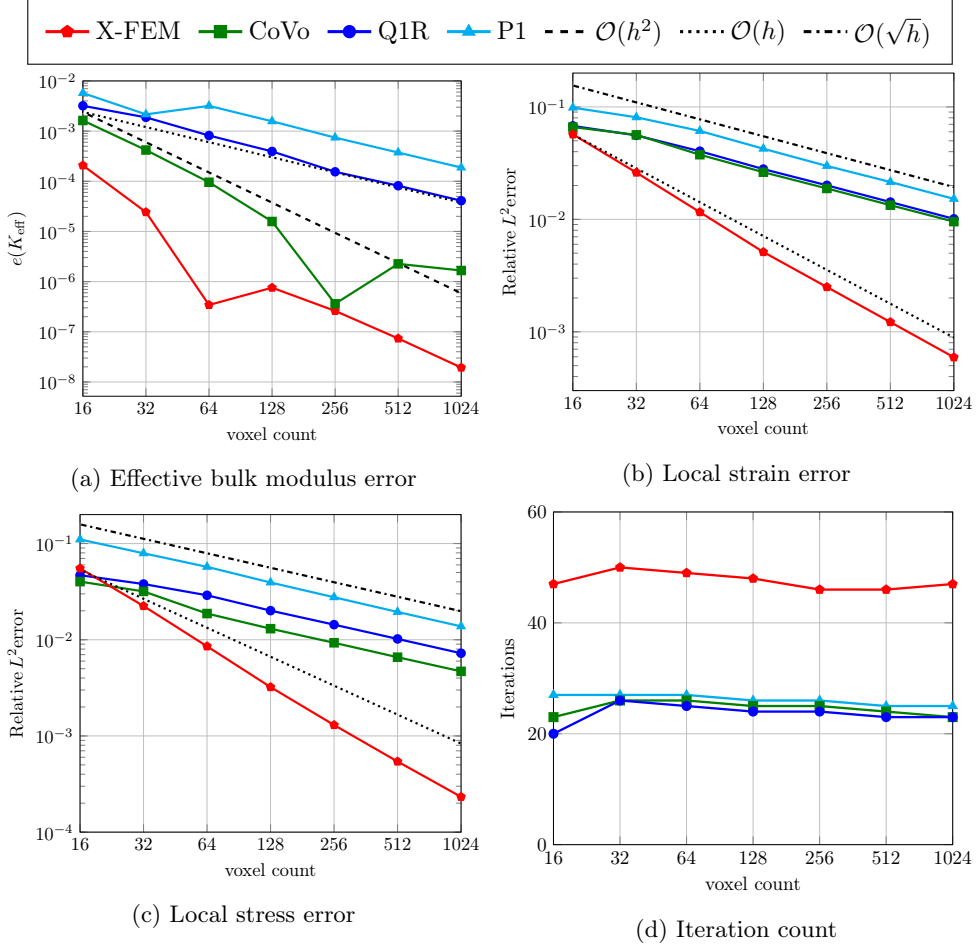


Figure 6: Accuracy and iteration count in Hashin's neutral inclusion.

With the analytical solution at hand, we compute the relative error in the effective bulk modulus using eq. (4.1). The resulting errors with respect to the mesh parameter h are shown in Fig. 6(a). We observe that the relative error in the effective bulk modulus is lowest for X-FEM at all resolutions. Moreover, a decrease in the error at the rate $\mathcal{O}(h^2)$ is observed as the mesh parameter decreases, which is consistent with previous observations on the convergence of error in the energy norm for X-FEM [65, Fig. 6]. The CoVo discretization shows the second-lowest error in the effective bulk modulus. Surprisingly, for CoVo, the error in the bulk modulus of Hashin's neutral inclusion decreases superlinearly with increasing resolution, which is not the case for more complex microstructures, compare Lendvai and Schneider [48, Fig. 11B-C]. The analytical solution of Hashin's neutral inclusion is independent of the Poisson's ratios, but depends on the phases bulk moduli. The bulk modulus is a measure of the infinitesimal pressure increase relative to the resulting decrease of the volume. One possible reason for the superlinear error

convergence of the CoVo discretization in the bulk modulus of Hashin's neutral inclusion is CoVo's ability to accurately approximate the volume fraction. At all resolutions, the Q1R discretization and the P1 discretization show the highest error in the effective bulk modulus at all resolutions, following the rate $\mathcal{O}(h)$ with decreasing mesh parameter.

To quantify the error in the local fields, the relative L^2 -error in the local strain and stress fields to the exact solution is computed based on eq. (4.1) and eq. (4.2). In general, we observe similar trends for the local strain in Fig. 6(b) and the local stress in Fig. 6(c). In both cases, X-FEM shows the least error at most resolutions and a linear error convergence with decreasing mesh parameter is observed. The rate $\mathcal{O}(h)$ coincides with the rate that is achieved by *interface-conforming* FEM with linear shape functions [39, Theorem 5.4.8; 40, p.190]. The P1, Q1R and CoVo discretization, show only a square root convergence rate in the relative L^2 -error in the local strain and stress fields with decreasing mesh parameter. The highest error is observed for the P1 discretization followed by the Q1R and the CoVo discretization. We observe that for the conforming Galerkin discretizations, namely, the X-FEM, the P1 and the Q1R discretizations, the error in the effective bulk modulus decreases with the squared rate of the L^2 -error in the local strain and stress fields, as proved by the inequalities (4.3), (4.4). However, our observations on the error convergence rates of CoVo demonstrate that the inequalities (4.3), (4.4) may not be fulfilled if no conforming Galerkin discretization is used.

Numerical efficiency

For the iteration count until convergence of linear CG, we observe in Fig. 6(d) that the discretizations P1, Q1R and CoVo require around 15-19 iterations. In contrast, for X-FEM 28-31 iterations are required until convergence. Nevertheless, the iteration counts of X-FEM appear stable with respect to the mesh parameter.

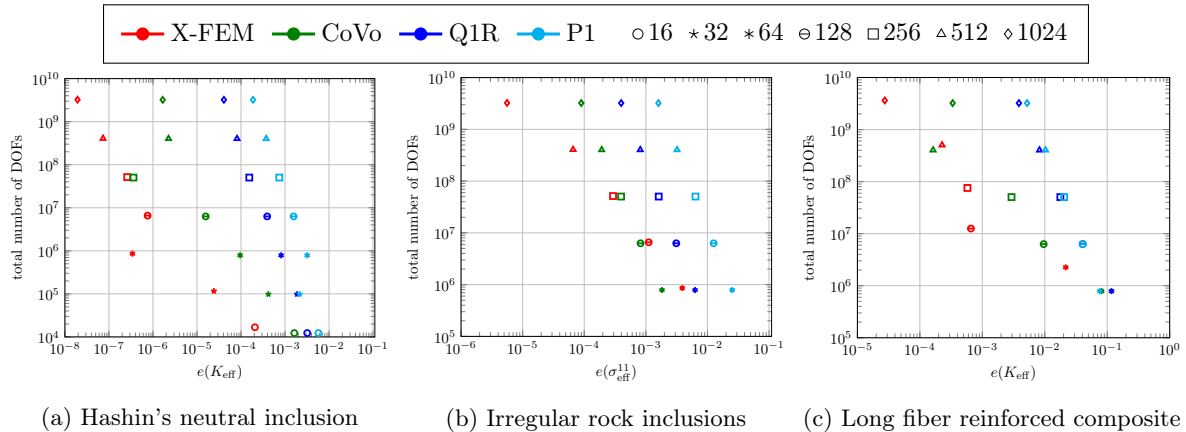


Figure 7: Total number of *dofs* versus relative error.

To assess the efficiency of the discretizations, not only the iteration count, but also the number of degrees of freedom is relevant. For all discretizations considered, three degrees of freedom per node are required for each standard FE field. In the X-FEM discretization, three additional degrees of freedom (*dofs*) are added to the approximation space for each enriched node. To evaluate whether the higher accuracy of X-FEM justifies its increased number of *dofs*, we show in Fig. 7(a) the total number of *dofs* per field versus the relative error in the effective bulk modulus. At low resolutions, the difference in the number of *dofs* is pronounced, i.e., at voxel count $N = 16$, X-FEM requires 36% more *dofs* than the other discretizations. However, this difference decreases quadratically with increasing voxel count so that

at voxel count $N = 1024$ the difference is only 0.5%. Above all, we observe that for a desired accuracy of 0.1%, X-FEM offers the cheapest result in terms of *dofs*: For X-FEM, a study with voxel count $N = 16$ is sufficient to reach an error in the effective bulk modulus that is below 0.1%. To reach an accuracy below 0.1%, with CoVo or Q1R a study with voxel count $N = 32$ would be necessary, for P1 even a voxel count $N = 64$ would be required. We conclude that, for Hashin's neutral inclusion, the X-FFT solver offers the best balance of accuracy and efficiency across all resolutions.

Contrast dependency

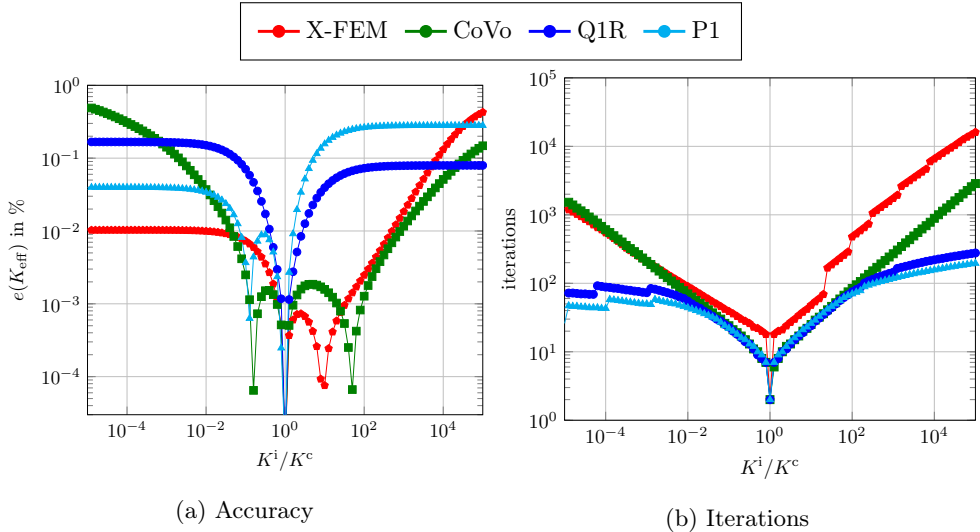


Figure 8: Contrast study for Hashin's neutral inclusion at voxel count $N = 128$.

To analyze the effect of the material contrast on the accuracy, we compute the error of the effective bulk modulus for different ratios of the bulk moduli of the inclusion and coating phase, denoted by the parameter K^i/K^c . If the parameter K^i/K^c is low, we model an almost void inclusion, whereas a high bulk moduli ratio denotes an almost rigid inclusion. The connection of the parameter K^i/K^c with the material contrast κ is given by the relation

$$\kappa = \begin{cases} K^i/K^c, & \text{if } K^i \geq K^c, \\ K^c/K^i, & \text{if } K^c > K^i. \end{cases} \quad (4.5)$$

In Fig. 8(a), we show the error of the effective bulk modulus in Hashin's neutral inclusion at voxel count $N = 128$ for different parameters K^i/K^c . We observe that X-FEM shows the least error in the effective bulk modulus for almost void inclusions, i.e., at parameters $K^i/K^c \in [10^{-5}, 0.04]$ and at moderately stiff inclusions, i.e., at parameters $K^i/K^c \in (1; 25]$. For moderately compliant inclusions, i.e., at parameters $K^i/K^c \in [0.04; 1)$ and for stiff inclusions, i.e., at parameters $K^i/K^c \in (25, 2 \cdot 10^4]$, CoVo shows the least error in the effective bulk modulus. If the bulk moduli of the inclusion and the coating phase coincide, Hashin's neutral inclusion reduces to a homogeneous microstructure, such that all discretizations perform equally accurate. For almost rigid inclusions, i.e., at parameters $K^i/K^c \in (2 \cdot 10^4, 10^5]$, Q1R shows the least error in the effective bulk modulus.

The material contrast is expected to have significant impact on the convergence rate of the residual (3.15), as the condition number of the preconditioned systems is bounded by a contrast-dependent constant for all considered discretizations. We assess the influence of the specific discretization on this behavior. To that

end, we investigate the iteration count for Hashin's neutral inclusion at voxel count $N = 128$ for different ratios of the bulk moduli of the inclusion and coating phase. Our results, shown in Fig. 8(b), indicate that the iteration count of Q1R is smallest for small material contrasts, while the iteration count of P1 is smallest for large material contrasts. For small material contrasts, the iteration count of CoVo is close to that of Q1R, whereas for large material contrasts it increases considerably. For nearly rigid inclusions with parameter $K^i/K^c = 10^5$, CoVo requires 2859 iterations until reaching the desired tolerance of 10^{-7} . For X-FEM, the increase in the iteration count is even higher for nearly rigid inclusions, so that, with the parameter $K^i/K^c = 10^5$ the iteration count increases to 16081 iterations. For inclusions with material properties similar to those of voids, the iteration count of X-FEM is slightly below that of CoVo. At the parameter $K^i/K^c = 10^{-5}$, X-FEM requires 1316 iterations and CoVo requires 1696 iterations until reaching the desired tolerance. For all discretizations considered, the iteration count appears to increase at the rate $\mathcal{O}(\sqrt{\kappa})$ as the material contrast increases, which coincides with the expected rate for linear CG [8].

4.3 Smooth rock inclusions in a cemented matrix

Microstructure

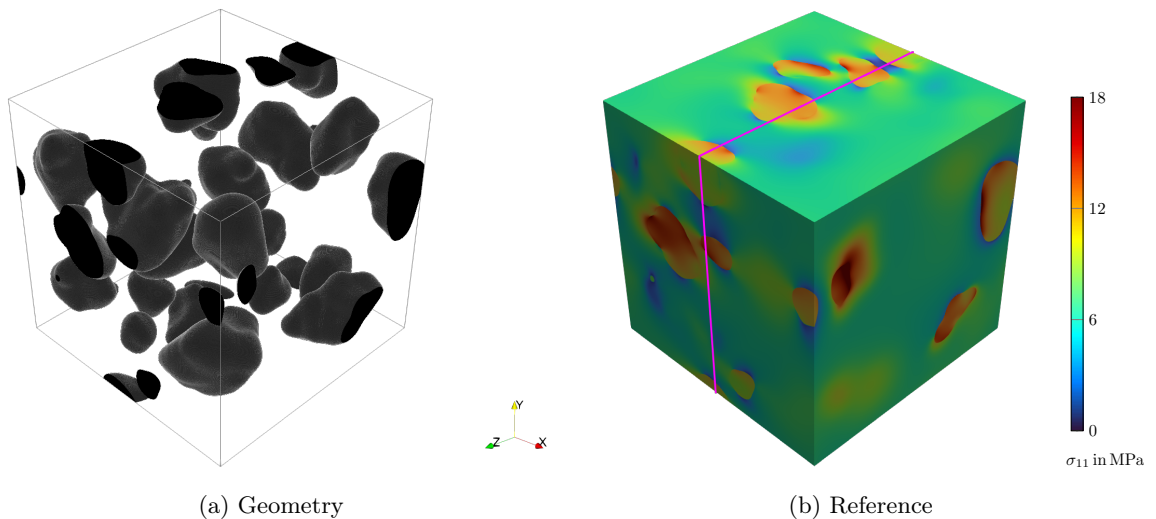


Figure 9: Geometry and reference solution of the rock-cement microstructure.

To analyze whether the X-FFT solver maintains its accuracy and efficiency for more complex microstructures, we consider smooth rock inclusions in a cemented matrix in this subsection. The respective microstructure was generated by forming each grain as a cluster of spheres and packing the grains using the Mechanical Contraction Method [72, 78]. In this context, we apply an exponential smoothing of the grains' surface [103]. Due to the description as a cluster of spheres, the level set description of each particle is naturally available. The resulting microstructure is shown in Fig. 9(a) with an edge length $512\mu\text{m}$ and features a volume fraction of 15% of the grains. We use the material parameters of Lin et al. [104, Tab.3] for the cemented matrix (gypsum) and the rocks (Portland cement) and prescribe unidirectional loading with the strain $\bar{\varepsilon}_{11} = 0.1\%$. The desired tolerance of the stopping criterion (3.14) of the solver is set to 10^{-5} for this study.

	Cemented matrix (Gypsum)	Rocks (Portland cement)
Young's modulus	6 GPa	35 GPa
Poisson's ratio	0.3	0.22

Table 2: Material parameters for the rock-cement microstructure.

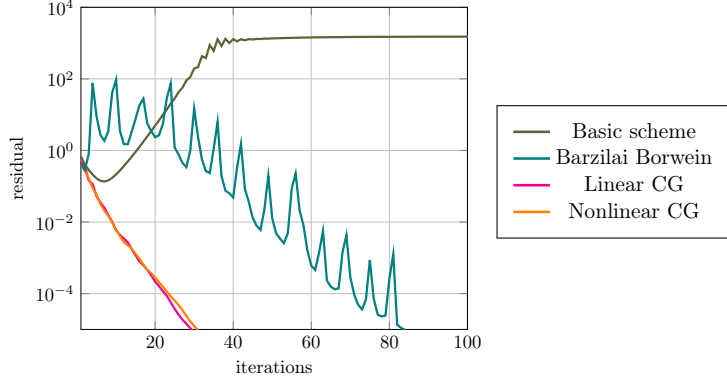


Figure 10: Solver convergence for X-FEM at voxel count $N = 128$ for the rock-cement microstructure.

Solution scheme

We compare the convergence of linear CG [19], the basic scheme [1, 2], the Barzilai Borwein scheme [20], and the nonlinear CG scheme [98], for X-FEM at voxel count $N = 128$. The convergence of the residual (3.15) with the iteration count of each solver is shown in Fig. 10. The residual of the basic scheme increases after reaching a minimum value and remains constant after approximately 50 iterations. This behavior indicates that the chosen step size (3.17) is suboptimal, i.e., too large. The Barzilai Borwein scheme shows its characteristic non-monotonically converging behavior and reaches the desired tolerance 10^{-5} at iteration count 85. The nonlinear CG scheme requires 32 iterations to reach the desired tolerance, while linear CG achieves this in 31 iterations. Based on these results, we choose to use linear CG for this section.

Accuracy

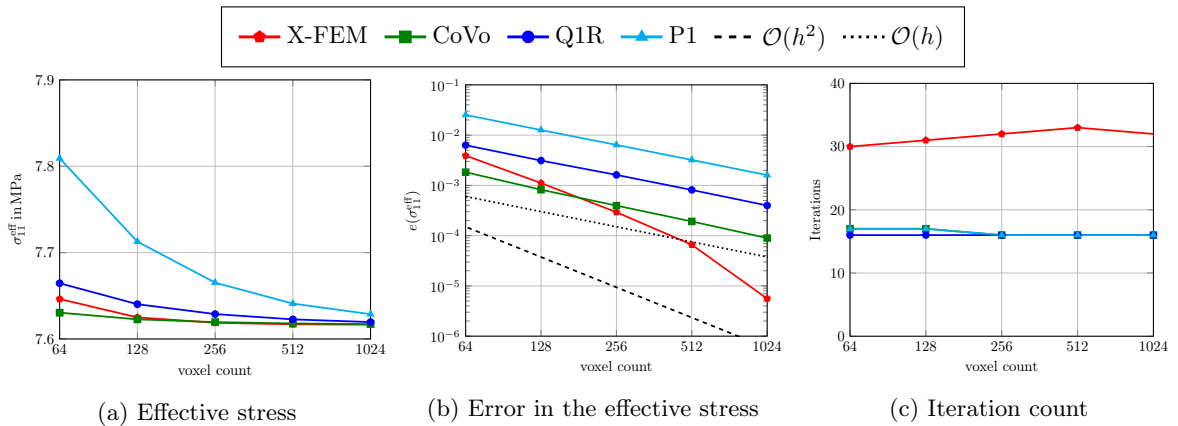


Figure 11: Effective stress and iteration count for the rock-cement microstructure.

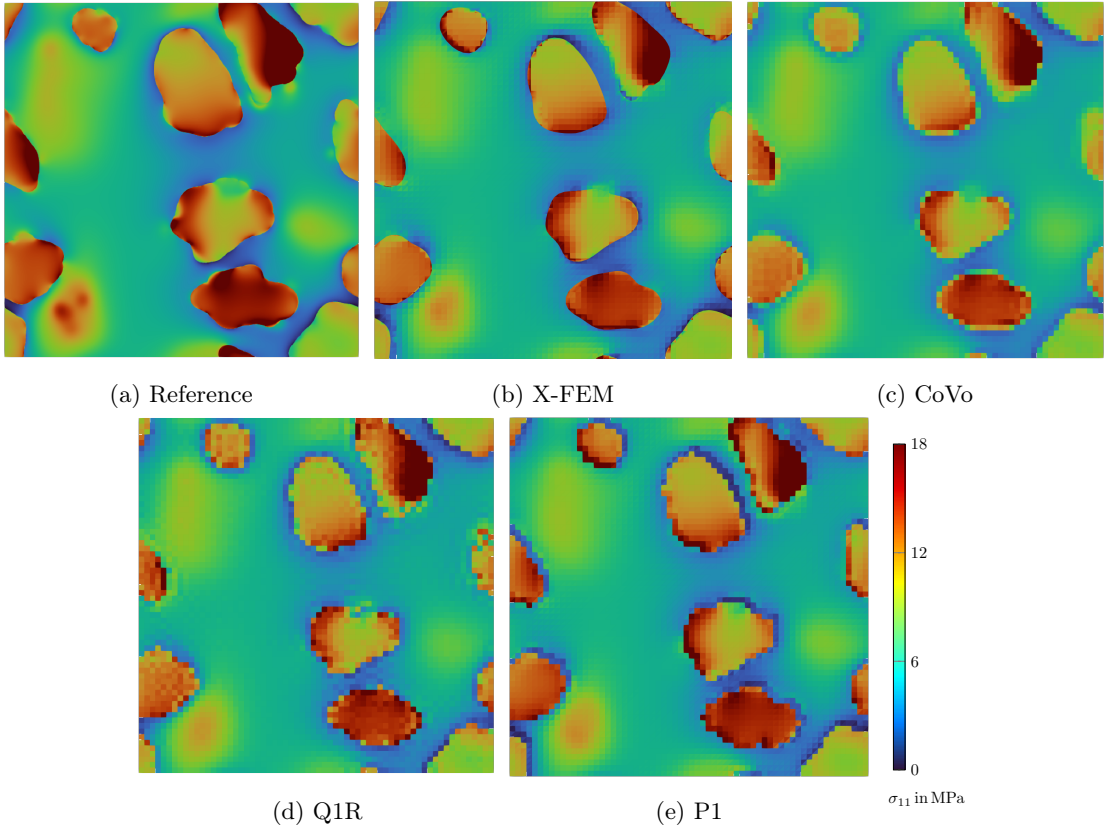


Figure 12: Slice in the y-z plane of the local stress field at voxel count $N = 64$ for the rock-cement microstructure.

Fig. 11(a) shows the xx-component of the effective stress. We observe that the P1 discretization strongly overestimates the effective stress at low resolutions, followed by the Q1R discretization. The X-FEM discretization and the CoVo discretization approximate the xx-component of the effective stress the most accurately at the lowest resolution considered. As the voxel count per axis increases, the X-FEM discretization appears to converge faster in the effective stress than the CoVo discretization. To investigate the accuracy of the effective stress approximations more closely, we consider the relative error in the xx-component of the effective stress with reference to the X-FEM result at voxel count $N = 1200$ in Fig 11(b). We observe that at low resolutions, the CoVo discretization approximates the xx-component of the effective stress the most accurately. However, for voxel counts greater than 128 voxels per axis, the X-FEM discretization approximates the xx-component of the effective stress the closest. Moreover, for X-FEM, we observe a quadratically decreasing error with increasing resolution, whereas for the CoVo, the P1 and the Q1R discretization the decrease in the error is linear. The convergence rates confirm those identified for Hashin's neutral inclusion in section 4.2.

We qualitatively analyze the local accuracy at the voxel count $N = 64$. For each discretization, the local fields are resolved and interpolated using the finite elements discussed in Tab. 1. For X-FEM, we show the interpolation based on the additional shape functions in the subtetrahedra used for the numerical integration. In Fig. 12, the xx-component of the local stress field is analyzed at the location that is indicated by the pink box in Fig. 9(b). The reference solution is provided by an X-FEM discretization at voxel count $N = 1200$. In Fig. 12, we observe that the X-FEM discretization at voxel count $N = 64$ approximates the reference solution the most closely. Due to the lower resolution, the X-FEM discretization at voxel count $N = 64$ does not capture all the details of the rock inclusion, but it detects the general

shape and accurately measures the stress magnitude, except in some small areas. The CoVo, Q1R and P1 discretization do not detect the outlines as accurately as the X-FEM discretization. In addition, the Q1R discretization shows checkerboarding, i.e., solution artifacts known from the literature [30, 34, 35]. As the CoVo discretization at hand uses the Q1R discretization in voxels that do not contain an interface it is not surprising that for the CoVo discretization slight solution artifacts are observed as well.

For the conforming Galerkin discretizations, namely, the X-FEM and the P1 discretization, inequality (4.3) holds, such that the error in the local strain and stress fields is bounded from above by the square root of the error in the effective stress. As we observed in Fig 11(b) that for P1 the error in the effective stress decreases with the rate $\mathcal{O}(h)$ with decreasing mesh parameter, the local stress must decreases with the rate $\mathcal{O}(\sqrt{h})$ with decreasing mesh parameter. For X-FEM, the error in the effective stress decreases at the rate $\mathcal{O}(h^2)$, implying that the error in the local stress decreases at the rate $\mathcal{O}(h)$ as the mesh parameter decreases. This rate is identical to the rate of interface-conforming FEM with linear shape functions [39, Theorem 5.4.8; 40, p.190]. Therefore, our X-FFT solver achieves interface-conforming accuracy also for smooth rock inclusions in a cemented matrix.

Numerical efficiency

In Fig. 11(c) we observe that the CoVo, the P1 and the Q1R discretization require an iteration count of 16-17 iterations in linear CG until the residual (3.15) reaches the desired tolerance of 10^{-5} . In contrast, the X-FEM discretization shows an iteration count between 30-33 iterations, i.e, approximately twice as many iterations are required to reach the desired tolerance compared to the other discretizations.

To assess the effort in terms of *dofs*, we show in Fig. 7(b) the total number of *dofs* per field versus the relative error in the xx-component of the effective stress. We observe that for a desired accuracy of 0.1% the CoVo discretization at $N = 64$ offers the cheapest solution in terms of *dofs*. To reach an accuracy below 0.01%, the X-FEM discretization at $N = 512$ offers the cheapest solution in terms of *dofs*. Thus, for the smooth rock inclusion microstructure the question of which discretization offers the best balance of accuracy and efficiency depends on the desired level of accuracy. However, the results of this section confirm that our X-FFT solver may achieve interface-conforming accuracy also for complex microstructures with smooth inclusions while maintaining numerical efficiency.

4.4 Long fiber reinforced composite

Microstructure

For the final example treated in this manuscript, we examine a microstructure with non-smooth interfaces, namely a long fiber reinforced composite microstructure. We use the fused sequential addition and migration method of Lauff et al. [105, 106] to generate the microstructure shown in Fig. 13(a). We assume a cell length of $64\mu\text{m}$, a fiber diameter of $2.5\mu\text{m}$, a fiber length of $252.96\mu\text{m}$ and use exact closure from the second-order fiber orientation tensor $\text{diag}(0.77, 0.17, 0.6)$. The reached fiber volume fraction is 17.93 vol-%, the average fiber curvature is $0.0718\mu\text{m}^{-1}$ and the maximum bending angle is 45.80° . We consider a polypropylene matrix and E-glass fibers with the material parameters given in Tab. 3 and prescribe unidirectional loading with the strain $\bar{\varepsilon}_{11} = 0.1\%$.

	Polypropylene matrix	E-glass fibers
Young's modulus	1.25 GPa	72 GPa
Poisson's ratio	0.35	0.22

Table 3: Material parameters [107, 108] for the long fiber reinforced composite.

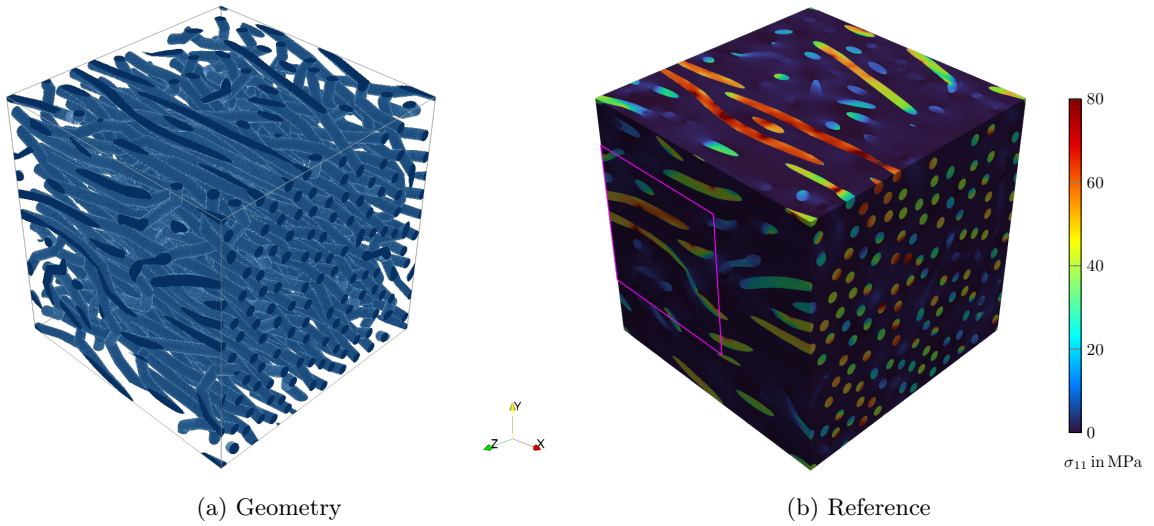


Figure 13: Geometry and reference solution of the long fiber reinforced composite.

Solution scheme

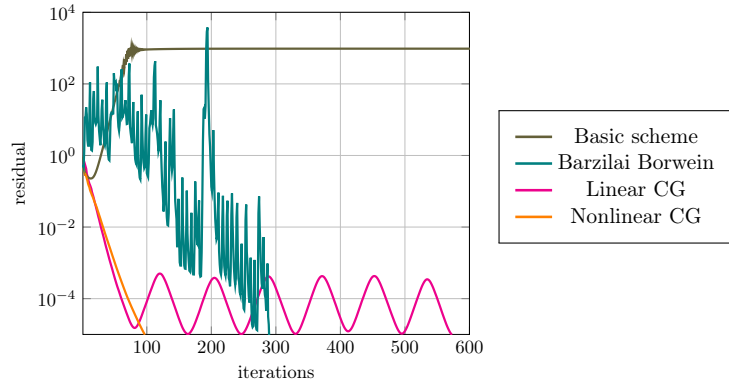


Figure 14: Solver convergence for X-FEM at voxel count $N = 128$ for the long fiber reinforced composite.

To select the solution scheme for this section, we compare the convergence of linear CG [19], the basic scheme [1, 2], the Barzilai Borwein scheme [20], and the nonlinear CG scheme [98], for X-FEM at voxel count $N = 128$. Fig. 14 shows the convergence of the residual (3.15) with the iteration count of each solver. We observe that the residual of the basic scheme increases after reaching a minimum value and remains constant after approximately 100 iterations. Thus, the choice of the step size (3.17) for the basic scheme is not recommended. The Barzilai Borwein scheme shows its characteristic non-monotonic convergence behavior and reaches the desired tolerance of 10^{-5} at iteration count 291. The linear CG scheme shows some sinusoidal behavior and requires 574 iterations to reach the desired tolerance. In contrast, the nonlinear CG scheme converges monotonically and reaches the desired tolerance after 98 iterations. Although we still consider linear elasticity, the non-smooth fiber geometry appears to affect the conditioning of the X-FEM system so that nonlinear CG shows faster convergence than linear CG for the long fiber reinforced composite. Therefore, we select nonlinear CG as the solver for this section.

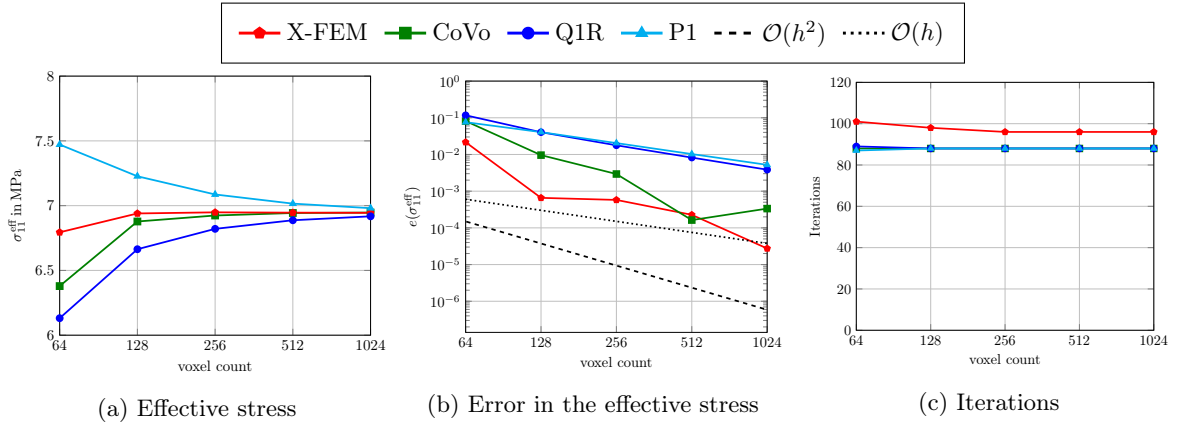


Figure 15: Effective stress and iteration count for the long fiber reinforced composite.

Accuracy

The xx-component of the effective stress is shown in Fig. 15(a). X-FEM appears to most accurately approximate the xx-component of the effective stress overall. For a more detailed analysis we show in Fig. 15(b) the relative error in the xx-component of the effective stress, where we select X-FEM at voxel count $N = 1200$ as reference solution. We observe that X-FEM achieves the lowest error at most resolutions, followed by CoVo. P1 and Q1R yield the highest errors. As expected, the errors of P1, Q1R, and CoVo converge linearly. However, the X-FEM errors also converge less than quadratically for the long fiber reinforced composite. This subquadratic convergence rate in X-FEM is due to the non-smooth fiber geometry. Even when refining the mesh, the modified abs enrichment may not accurately approximate the non-smooth fiber ends. For X-FEM with the modified abs enrichment, we expect the error in the xx-component of the effective stress to increase with the number of non-smooth geometries in the microstructure. It would be beneficial to explore possibilities to extend the current X-FFT framework to enable quadratic error convergence for non-smooth interfaces in the future.

To evaluate the quality of the local fields, we assess the xx-component of the local stress field for each discretization and compare it to a reference solution provided by X-FEM with at voxel count $N = 1200$. The pink box in the reference solution, shown in Fig. 13(b), encloses the image section that we analyze below. In Fig. 16, we observe that X-FEM with a voxel count $N = 64$ approximates the local stress field of the reference solution rather closely. In contrast, CoVo significantly underestimates the xx-component of the local stress and offers only a crude approximation of the fibers. Furthermore, CoVo and Q1R display checkerboarding artifacts, as discussed in Fig. 12. For Q1R, the stress values are in the correct order of magnitude, but the fiber geometry is not approximated correctly. The latter is also visible for P1 combined with an overestimation of the xx-component of the local stress in the fibers.

Numerical efficiency

The iteration count until convergence of nonlinear CG is shown in Fig. 15(c). We observe that P1, Q1R and CoVo require 87-89 iterations to converge. For X-FEM, an increased iteration count of 98-101 iterations is observed. We note that the iteration count of X-FEM could be reduced by improving the selection of the step size (3.17).

In Fig. 7(c) the computational effort in terms of degrees of freedom (*dofs*) per field as a measure of the memory footprint is analyzed. We observe that the X-FEM discretization at voxel count $N = 128$ provides the most memory-efficient solution for achieving a desired accuracy of 0.1%. Furthermore,

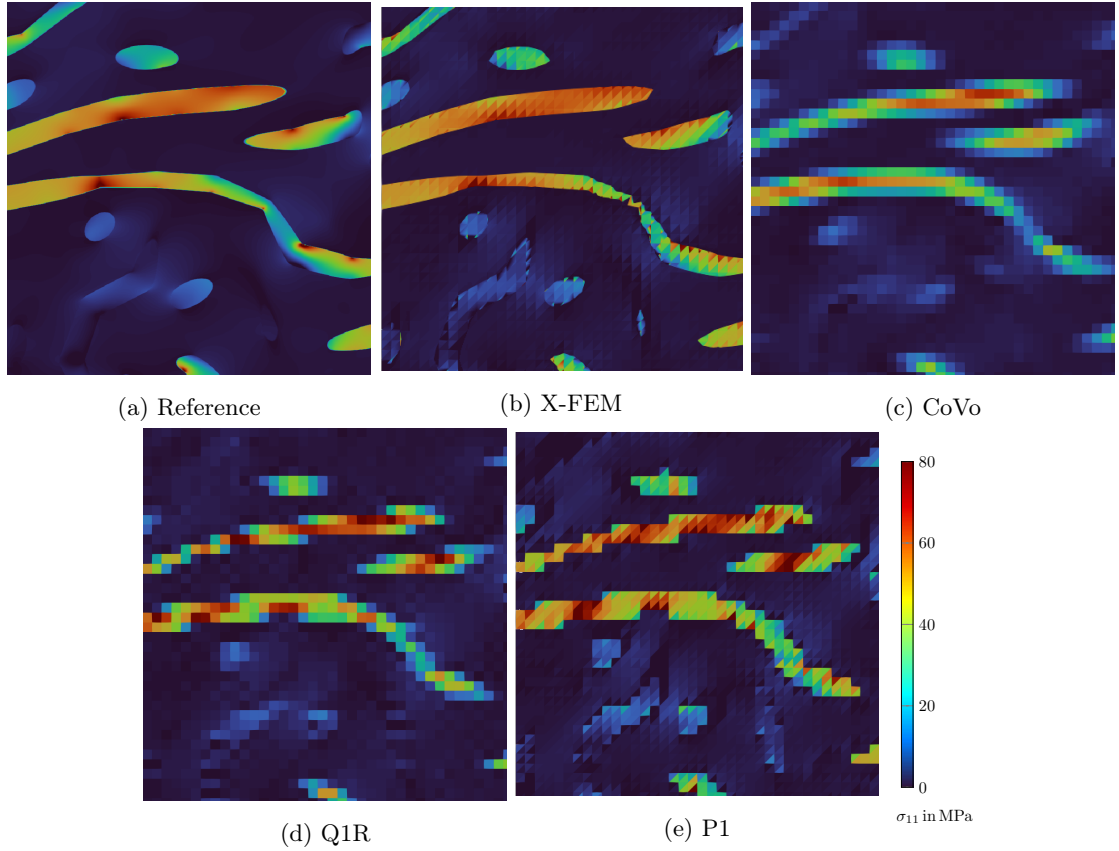


Figure 16: Zoomed view of local stress field at voxel count $N = 64$ for the long fiber reinforced composite.

to reach an accuracy below 0.01%, the X-FEM discretization at voxel count $N = 1024$ offers the most efficient solution in terms of *dofs*. Overall, the X-FEM method approximates the local and effective stress fields the most accurately for the long fiber-reinforced composite in question. However, we found that non-smooth interfaces can degrade the conditioning of the X-FEM system and reduce its accuracy.

5 Conclusion and perspectives

The work at hand introduced a three-dimensional X-FFT solver specifically designed for solving computational homogenization problems in linear elasticity with finite material contrast. This X-FFT solver achieves interface-conforming accuracy for matrix-inclusion problems with smooth interface geometry, while maintaining the numerical efficiency of FFT-based methods. Our computational studies demonstrated that interface-conforming convergence rates may be achieved not only for simplistic examples, such as Hashin’s neutral inclusion, but also for more complex microstructures with smooth interfaces, including smooth rock inclusions in a cemented matrix. Despite featuring an increased iteration count and memory footprint compared to other discretizations in FFT-based methods, the X-FFT solver still offers the best balance between accuracy and numerical efficiency in most cases. The X-FFT solver is particularly useful for those interested in local fields because it produces remarkably accurate local fields, even at low resolutions.

To the best of our knowledge, applying the concept of strongly stable X-FEM [70] to three-dimensional solid mechanics is novel, and using an FFT-based method to solve a mechanical homogenization problem discretized via X-FEM is an innovative strategy. We highlight that other X-FEM applications could

benefit from using FFT-based solvers as well, e.g., modeling the propagation of cracks in heterogeneous microstructures [55]. Furthermore, improving the current X-FFT framework to achieve interface-conforming accuracy in matrix-inclusion problems with non-smooth interfaces, such as fiber ends, would be beneficial. Based on the strategy discussed in Kästner et al. [109], the X-FFT solver may be extended to allow for two interfaces per element. Extending it to nonlinear materials would also be feasible, although the large number of integration points could present a challenge, so that advanced strategies [110] for dealing with internal variables might become necessary. Moreover, improving the choice of the step size is recommended when extending it to nonlinear materials as linear CG is not suited for nonlinear systems.

Acknowledgements

The authors would like to gratefully acknowledge the support of the European Research Council within the Horizon Europe program, project 101040238.

Data availability statement

The data that support the findings of this study are available from the corresponding author upon reasonable request.

A Error bounds in conforming Galerkin methods

In this appendix, we derive the inequalities (4.3) and (4.4), which hold for conforming Galerkin methods. For linear elasticity, we consider a linear mapping between strain and stress fields based on the local stiffness matrix $\mathbb{C} \in \text{Lin}(\text{Sym}(3))$, where the inequalities

$$C_- \|\boldsymbol{\varepsilon}\|^2 \leq \boldsymbol{\varepsilon} : \mathbb{C} : \boldsymbol{\varepsilon} \leq C_+ \|\boldsymbol{\varepsilon}\|^2 \quad \text{for all } \boldsymbol{\varepsilon} \in \text{Sym}(3) \quad (\text{A.1})$$

hold for all points $\boldsymbol{x} \in Y$, with the positive constants C_-, C_+ . Under the assumption of exact integration over the cell Y , which is fulfilled by conforming Galerkin methods, the inequalities

$$C_- \|\boldsymbol{\varepsilon}\|_{L^2}^2 \leq \langle \boldsymbol{\varepsilon} : \mathbb{C} : \boldsymbol{\varepsilon} \rangle_Y \leq C_+ \|\boldsymbol{\varepsilon}\|_{L^2}^2 \quad (\text{A.2})$$

result for all fields $\boldsymbol{\varepsilon} \in L^2(Y; \text{Sym}(d))$. We consider the difference between the simulated strain $\boldsymbol{\varepsilon}_h$ and the exact strain $\boldsymbol{\varepsilon}_*$. For this strain difference, the inequalities (A.2) take the form

$$C_- \|\boldsymbol{\varepsilon}_* - \boldsymbol{\varepsilon}_h\|_{L^2}^2 \leq \langle (\boldsymbol{\varepsilon}_* - \boldsymbol{\varepsilon}_h) : \mathbb{C} : (\boldsymbol{\varepsilon}_* - \boldsymbol{\varepsilon}_h) \rangle_Y \leq C_+ \|\boldsymbol{\varepsilon}_* - \boldsymbol{\varepsilon}_h\|_{L^2}^2. \quad (\text{A.3})$$

Based on Schneider [100, eq.(18)], we may rewrite the cell-averaged error of the elastic energy in the form

$$\langle (\boldsymbol{\varepsilon}_* - \boldsymbol{\varepsilon}_h) : \mathbb{C} : (\boldsymbol{\varepsilon}_* - \boldsymbol{\varepsilon}_h) \rangle_Y = \langle \boldsymbol{\varepsilon}_* : \mathbb{C} : \boldsymbol{\varepsilon}_* \rangle_Y - \langle \boldsymbol{\varepsilon}_h : \mathbb{C} : \boldsymbol{\varepsilon}_* \rangle_Y. \quad (\text{A.4})$$

For both terms on the right-hand side of the equation above, we follow the approach discussed in Schneider [100, eq.(19)]. More precisely, we use the definition of the exact strain

$$\boldsymbol{\varepsilon}_* = \bar{\boldsymbol{\varepsilon}} + \nabla^s \boldsymbol{u}_*, \quad (\text{A.5})$$

apply integration by parts and use the validity of the balance of linear momentum for the exact strain such that the relation

$$\begin{aligned}
\langle \boldsymbol{\varepsilon}_* : \mathbb{C} : \boldsymbol{\varepsilon}_* \rangle_Y - \langle \boldsymbol{\varepsilon}_h : \mathbb{C} : \boldsymbol{\varepsilon}_* \rangle_Y &= \langle \boldsymbol{\varepsilon}_* : \mathbb{C} : \boldsymbol{\varepsilon}_* \rangle_Y - \langle \boldsymbol{\varepsilon}_* : \mathbb{C} : \boldsymbol{\varepsilon}_h \rangle_Y \\
&= \langle (\bar{\boldsymbol{\varepsilon}} + \nabla^s \mathbf{u}_*) : \mathbb{C} : \boldsymbol{\varepsilon}_* \rangle_Y - \langle (\bar{\boldsymbol{\varepsilon}} + \nabla^s \mathbf{u}_*) : \mathbb{C} : \boldsymbol{\varepsilon}_h \rangle_Y \\
&= \bar{\boldsymbol{\varepsilon}} \langle \mathbb{C} : \boldsymbol{\varepsilon}_* \rangle_Y - \bar{\boldsymbol{\varepsilon}} \langle \mathbb{C} : \boldsymbol{\varepsilon}_h \rangle_Y \\
&= \bar{\boldsymbol{\varepsilon}} : \mathbb{C}_*^{\text{eff}} : \bar{\boldsymbol{\varepsilon}} - \bar{\boldsymbol{\varepsilon}} : \mathbb{C}_h^{\text{eff}} : \bar{\boldsymbol{\varepsilon}}
\end{aligned}$$

results with the simulated effective stiffness $\mathbb{C}_h^{\text{eff}}$ and the exact effective stiffness $\mathbb{C}_*^{\text{eff}}$. In summary, the equation

$$\langle (\boldsymbol{\varepsilon}_* - \boldsymbol{\varepsilon}_h) : \mathbb{C} : (\boldsymbol{\varepsilon}_* - \boldsymbol{\varepsilon}_h) \rangle_Y = \bar{\boldsymbol{\varepsilon}} : (\mathbb{C}_*^{\text{eff}} - \mathbb{C}_h^{\text{eff}}) : \bar{\boldsymbol{\varepsilon}} \quad (\text{A.6})$$

holds for the cell-averaged error of the elastic energy, so that the inequalities (A.3) take the form

$$C_- \|\boldsymbol{\varepsilon}_* - \boldsymbol{\varepsilon}_h\|_{L^2}^2 \leq \bar{\boldsymbol{\varepsilon}} : (\mathbb{C}_*^{\text{eff}} - \mathbb{C}_h^{\text{eff}}) : \bar{\boldsymbol{\varepsilon}} \leq C_+ \|\boldsymbol{\varepsilon}_* - \boldsymbol{\varepsilon}_h\|_{L^2}^2. \quad (\text{A.7})$$

The error in the effective elastic energy may thus be bounded from above by a value which is proportional to the quadratic error in the local strain fields via the relation

$$\bar{\boldsymbol{\varepsilon}} : (\mathbb{C}_*^{\text{eff}} - \mathbb{C}_h^{\text{eff}}) : \bar{\boldsymbol{\varepsilon}} \leq C_+ \|\boldsymbol{\varepsilon}_* - \boldsymbol{\varepsilon}_h\|_{L^2}^2. \quad (\text{A.8})$$

Moreover, the error in the local strain fields may be bounded from above by a value which is proportional to the square root of the error in the effective elastic energy via the inequality

$$\|\boldsymbol{\varepsilon}_* - \boldsymbol{\varepsilon}_h\|_{L^2} \leq \sqrt{\frac{\bar{\boldsymbol{\varepsilon}} : (\mathbb{C}_*^{\text{eff}} - \mathbb{C}_h^{\text{eff}}) : \bar{\boldsymbol{\varepsilon}}}{C_-}}. \quad (\text{A.9})$$

References

- [1] H. Moulinec and P. Suquet, “A fast numerical method for computing the linear and nonlinear mechanical properties of composites,” *Comptes Rendus de l’Académie des sciences. Série II. Mécanique, physique, chimie, astronomie*, vol. 318, no. 11, pp. 1417–1423, 1994.
- [2] H. Moulinec and P. Suquet, “A numerical method for computing the overall response of nonlinear composites with complex microstructure,” *Computer Methods in Applied Mechanics and Engineering*, vol. 157, no. 1-2, pp. 69–94, 1998.
- [3] M. Frigo and S. G. Johnson, “The design and implementation of FFTW3,” *Proceedings of the IEEE*, vol. 93, no. 2, pp. 216–231, 2005.
- [4] L. Dalcin, M. Mortensen, and D. E. Keyes, “Fast parallel multidimensional FFT using advanced MPI,” *Journal of Parallel and Distributed Computing*, vol. 128, pp. 137–150, 2019.
- [5] Y. Chen, L. Gélébart, C. Chateau, M. Bornert, C. Sauder, and A. King, “Analysis of the damage initiation in a SiC/SiC composite tube from a direct comparison between large-scale numerical simulation and synchrotron X-ray micro-computed tomography,” *International Journal of Solids and Structures*, vol. 161, pp. 111–126, 2019.
- [6] R. A. Lebensohn and A. D. Rollett, “Spectral methods for full-field micromechanical modelling of polycrystalline materials,” *Computational Materials Science*, vol. 173, p. 109336, 2020.
- [7] S. Lucarini, M. V. Upadhyay, and J. Segurado, “FFT based approaches in micromechanics: fundamentals, methods and applications,” *Modelling and Simulation in Materials Science and Engineering*, vol. 30, no. 2, p. 023002, 2021.
- [8] M. Schneider, “A review of nonlinear FFT-based computational homogenization methods,” *Acta Mechanica*, vol. 232, no. 6, pp. 2051–2100, 2021.
- [9] C. Gierden, J. Kochmann, J. Waimann, B. Svendsen, and S. Reese, “A review of FE-FFT-based two-scale methods for computational modeling of microstructure evolution and macroscopic material behavior,” *Archives of Computational Methods in Engineering*, vol. 29, no. 6, pp. 4115–4135, 2022.
- [10] E. Kröner, *Statistical continuum mechanics*. Springer, 1972.

[11] R. Zeller and P. Dederichs, “Elastic constants of polycrystals,” *Physica Status Solidi (b)*, vol. 55, no. 2, pp. 831–842, 1973.

[12] S. Brisard and L. Dormieux, “Combining Galerkin approximation techniques with the principle of Hashin and Shtrikman to derive a new FFT-based numerical method for the homogenization of composites,” *Computer Methods in Applied Mechanics and Engineering*, vol. 217, pp. 197–212, 2012.

[13] F. Willot, B. Abdallah, and Y.-P. Pellegrini, “Fourier-based schemes with modified Green operator for computing the electrical response of heterogeneous media with accurate local fields,” *International Journal for Numerical Methods in Engineering*, vol. 98, no. 7, pp. 518–533, 2014.

[14] J. Vondřejc, J. Zeman, and I. Marek, “An FFT-based Galerkin method for homogenization of periodic media,” *Computers & Mathematics with Applications*, vol. 68, no. 3, pp. 156–173, 2014.

[15] M. Schneider, “Convergence of FFT-based homogenization for strongly heterogeneous media,” *Mathematical Methods in the Applied Sciences*, vol. 38, no. 13, pp. 2761–2778, 2015.

[16] N.-T. Nguyen, C. Licht, and J.-H. Kweon, “An efficient homogenization method using the trigonometric interpolation and the fast Fourier transform,” *Vietnam Journal of Mechanics*, vol. 33, no. 4, pp. 1–9, 2011.

[17] M. Kabel, T. Böhlke, and M. Schneider, “Efficient fixed point and Newton–Krylov solvers for FFT-based homogenization of elasticity at large deformations,” *Computational Mechanics*, vol. 54, no. 6, pp. 1497–1514, 2014.

[18] N. Mishra, J. Vondřejc, and J. Zeman, “A comparative study on low-memory iterative solvers for FFT-based homogenization of periodic media,” *Journal of Computational Physics*, vol. 321, pp. 151–168, 2016.

[19] J. Zeman, J. Vondřejc, J. Novák, and I. Marek, “Accelerating a FFT-based solver for numerical homogenization of periodic media by conjugate gradients,” *Journal of Computational Physics*, vol. 229, no. 21, pp. 8065–8071, 2010.

[20] M. Schneider, “On the Barzilai–Borwein basic scheme in FFT-based computational homogenization,” *International Journal for Numerical Methods in Engineering*, vol. 118, no. 8, pp. 482–494, 2019.

[21] D. Wicht, M. Schneider, and T. Böhlke, “On Quasi-Newton methods in fast Fourier transform-based micromechanics,” *International Journal for Numerical Methods in Engineering*, vol. 121, no. 8, pp. 1665–1694, 2020.

[22] S. Brisard and L. Dormieux, “FFT-based methods for the mechanics of composites: A general variational framework,” *Computational Materials Science*, vol. 49, no. 3, pp. 663–671, 2010.

[23] M. Zecevic and R. A. Lebensohn, “Approximation of periodic Green’s operator in real space using numerical integration and its use in fast Fourier transform-based micromechanical models,” *International Journal for Numerical Methods in Engineering*, vol. 122, no. 24, pp. 7536–7552, 2021.

[24] G. Bonnet, “Effective properties of elastic periodic composite media with fibers,” *Journal of the Mechanics and Physics of Solids*, vol. 55, no. 5, pp. 881–899, 2007.

[25] V. Monchiet, “Combining FFT methods and standard variational principles to compute bounds and estimates for the properties of elastic composites,” *Computer Methods in Applied Mechanics and Engineering*, vol. 283, pp. 454–473, 2015.

[26] J. Vondřejc, “Improved guaranteed computable bounds on homogenized properties of periodic media by the Fourier–Galerkin method with exact integration,” *International Journal for Numerical Methods in Engineering*, vol. 107, no. 13, pp. 1106–1135, 2016.

[27] C. Dorn and M. Schneider, “Lippmann–Schwinger solvers for the explicit jump discretization for thermal computational homogenization problems,” *International Journal for Numerical Methods in Engineering*, vol. 118, no. 11, pp. 631–653, 2019.

[28] K. S. Eloh, A. Jacques, and S. Berbenni, “Development of a new consistent discrete Green operator for FFT-based methods to solve heterogeneous problems with eigenstrains,” *International Journal of Plasticity*, vol. 116, pp. 1–23, 2019.

[29] F. Ernesti and M. Schneider, “A fast Fourier transform based method for computing the effective crack energy of a heterogeneous material on a combinatorially consistent grid,” *International Journal for Numerical Methods in Engineering*, vol. 122, no. 21, pp. 6283–6307, 2021.

[30] F. Willot, “Fourier-based schemes for computing the mechanical response of composites with accurate local fields,” *Comptes Rendus Mécanique*, vol. 343, no. 3, pp. 232–245, 2015.

[31] A. Vidyasagar, W. L. Tan, and D. M. Kochmann, “Predicting the effective response of bulk polycrystalline ferroelectric ceramics via improved spectral phase field methods,” *Journal of the Mechanics and Physics of Solids*, vol. 106, pp. 133–151, 2017.

[32] A. Finel, “A tetrahedron-based discretization for FFT-based computational homogenization with smooth solution fields,” *Computer Methods in Applied Mechanics and Engineering*, vol. 436, p. 117703, 2025.

[33] M. Schneider, D. Merkert, and M. Kabel, “FFT-based homogenization for microstructures discretized by linear hexahedral elements,” *International Journal for Numerical Methods in Engineering*, vol. 109, pp. 1461–1489, 2017.

[34] M. Leuschner and F. Fritzen, “Fourier-accelerated nodal solvers (FANS) for homogenization problems,” *Computational Mechanics*, vol. 62, pp. 359–392, 2018.

[35] M. Ladecký, R. J. Leute, A. Falsafi, I. Pultarová, L. Pastewka, T. Junge, and J. Zeman, “An optimal preconditioned FFT-accelerated finite element solver for homogenization,” *Applied Mathematics and Computation*, vol. 446, p. 127835, 2023.

[36] M. Schneider and D. Wicht, “Superconvergence of the effective Cauchy stress in computational homogenization of inelastic materials,” *International Journal for Numerical Methods in Engineering*, vol. 124, no. 4, pp. 959–978, 2023.

[37] C. Ye and E. T. Chung, “Convergence of trigonometric and finite-difference discretization schemes for FFT-based computational micromechanics,” *BIT Numerical Mathematics*, vol. 63, no. 1, p. 11, 2023.

[38] M. Schneider, “On the effectiveness of the Moulinec–Suquet discretization for composite materials,” *International Journal for Numerical Methods in Engineering*, vol. 124, no. 14, pp. 3191–3218, 2023.

[39] S. C. Brenner, *The mathematical theory of finite element methods*. Springer, 2008.

[40] T. J. Hughes, *The finite element method: linear static and dynamic finite element analysis*. Englewood Cliffs: Prentice-Hall, 1987.

[41] I. Ramière, “Convergence analysis of the Q1-finite element method for elliptic problems with non-boundary-fitted meshes,” *International Journal for Numerical Methods in Engineering*, vol. 75, no. 9, pp. 1007–1052, 2008.

[42] L. Gélibart and F. Ouaki, “Filtering material properties to improve FFT-based methods for numerical homogenization,” *Journal of Computational Physics*, vol. 294, pp. 90–95, 2015.

[43] M. Kabel, D. Merkert, and M. Schneider, “Use of composite voxels in FFT-based homogenization,” *Computer Methods in Applied Mechanics and Engineering*, vol. 294, pp. 168–188, 2015.

[44] L. Jabs, X. Zhou, L. Penter, S. Ihlenfeldt, and M. Schneider, “Microstructure modeling and computational micromechanics of glued metallic hollow-sphere composites,” *submitted*, 2025.

[45] B. Sterr, D. Wicht, A. Hrymak, M. Schneider, and T. Böhlke, “Homogenizing the viscosity of shear-thinning fiber suspensions with an FFT-based computational method,” *Journal of Non-Newtonian Fluid Mechanics*, vol. 321, p. 105101, 2023.

[46] B. Sterr, A. Hrymak, M. Schneider, and T. Böhlke, “Machine learning assisted discovery of effective viscous material laws for shear-thinning fiber suspensions,” *Computational Mechanics*, vol. 75, no. 1, pp. 51–69, 2025.

[47] C. Mareau and C. Robert, “Different composite voxel methods for the numerical homogenization of heterogeneous inelastic materials with FFT-based techniques,” *Mechanics of Materials*, vol. 105, pp. 157–165, 2017.

[48] J. Lendvai and M. Schneider, “Assumed strain methods in micromechanics, laminate composite voxels and level sets,” *International Journal for Numerical Methods in Engineering*, vol. 125, no. 11, p. e7459, 2024.

[49] S. Keshav, F. Fritzen, and M. Kabel, “FFT-based homogenization at finite strains using composite boxels (ComBo),” *Computational Mechanics*, vol. 71, no. 1, pp. 191–212, 2023.

[50] J. Lendvai and M. Schneider, “Accurate and consistent composite voxel methods for digital images in computational micromechanics,” *submitted*, 2025.

[51] M. Zecevic, R. A. Lebensohn, and L. Capolungo, “New large-strain FFT-based formulation and its application to model strain localization in nano-metallic laminates and other strongly anisotropic crystalline materials,” *Mechanics of Materials*, vol. 166, p. 104208, 2022.

[52] M. Zecevic, R. A. Lebensohn, and L. Capolungo, “Achieving geometric accuracy in FFT-based micromechanical models using conformal grid,” *Mechanics of Materials*, p. 105512, 2025.

[53] C. Bellis and R. Ferrier, “Numerical homogenization by an adaptive Fourier spectral method on non-uniform grids using optimal transport,” *Computer Methods in Applied Mechanics and Engineering*, vol. 419, p. 116658, 2024.

[54] F. Gehrig and M. Schneider, “An X-FFT Solver for Two-Dimensional Thermal Homogenization Problems,” *International Journal for Numerical Methods in Engineering*, vol. 126, no. 7, p. e70022, 2025.

[55] N. Moës, J. Dolbow, and T. Belytschko, “A finite element method for crack growth without remeshing,” *International Journal for Numerical Methods in Engineering*, vol. 46, no. 1, pp. 131–150, 1999.

[56] T. Belytschko and T. Black, "Elastic crack growth in finite elements with minimal remeshing," *International Journal for Numerical Methods in Engineering*, vol. 45, no. 5, pp. 601–620, 1999.

[57] J. Chessa and T. Belytschko, "An extended finite element method for two-phase fluids," *J. Appl. Mech.*, vol. 70, no. 1, pp. 10–17, 2003.

[58] J. Chessa and T. Belytschko, "An enriched finite element method and level sets for axisymmetric two-phase flow with surface tension," *International journal for numerical methods in engineering*, vol. 58, no. 13, pp. 2041–2064, 2003.

[59] C. Spieler, M. Kästner, J. Goldmann, J. Brummund, and V. Ulbricht, "XFEM modeling and homogenization of magnetoactive composites," *Acta Mechanica*, vol. 224, pp. 2453–2469, 2013.

[60] M. Kästner, S. Müller, J. Goldmann, C. Spieler, J. Brummund, and V. Ulbricht, "Higher-order extended FEM for weak discontinuities–level set representation, quadrature and application to magneto-mechanical problems," *International Journal for Numerical Methods in Engineering*, vol. 93, no. 13, pp. 1403–1424, 2013.

[61] J. H. Prevost and N. Sukumar, "Faults simulations for three-dimensional reservoir-geomechanical models with the extended finite element method," *Journal of the Mechanics and Physics of Solids*, vol. 86, pp. 1–18, 2016.

[62] D. Liu, S. J. van den Boom, A. Simone, and A. M. Aragón, "An interface-enriched generalized finite element formulation for locking-free coupling of non-conforming discretizations and contact," *Computational Mechanics*, vol. 70, no. 3, pp. 477–499, 2022.

[63] A. Simone, C. A. Duarte, and E. Van der Giessen, "A generalized finite element method for polycrystals with discontinuous grain boundaries," *International Journal for Numerical Methods in Engineering*, vol. 67, no. 8, pp. 1122–1145, 2006.

[64] N. Sukumar, D. L. Chopp, N. Moës, and T. Belytschko, "Modeling holes and inclusions by level sets in the extended finite-element method," *Computer Methods in Applied Mechanics and Engineering*, vol. 190, no. 46-47, pp. 6183–6200, 2001.

[65] N. Moës, M. Cloirec, P. Cartraud, and J.-F. Remacle, "A computational approach to handle complex microstructure geometries," *Computer Methods in Applied Mechanics and Engineering*, vol. 192, no. 28-30, pp. 3163–3177, 2003.

[66] T. Strouboulis, I. Babuška, and K. Copps, "The design and analysis of the generalized finite element method," *Computer Methods in Applied Mechanics and Engineering*, vol. 181, no. 1-3, pp. 43–69, 2000.

[67] T. Strouboulis, K. Copps, and I. Babuška, "The generalized finite element method: an example of its implementation and illustration of its performance," *International Journal for Numerical Methods in Engineering*, vol. 47, no. 8, pp. 1401–1417, 2000.

[68] I. Babuška, G. Caloz, and J. E. Osborn, "Special finite element methods for a class of second order elliptic problems with rough coefficients," *SIAM Journal on Numerical Analysis*, vol. 31, no. 4, pp. 945–981, 1994.

[69] T.-P. Fries and T. Belytschko, "The extended/generalized finite element method: an overview of the method and its applications," *International Journal for Numerical Methods in Engineering*, vol. 84, no. 3, pp. 253–304, 2010.

[70] I. Babuška, U. Banerjee, and K. Kergrene, "Strongly stable generalized finite element method: Application to interface problems," *Computer Methods in Applied Mechanics and Engineering*, vol. 327, pp. 58–92, 2017.

[71] S. Osher and J. A. Sethian, "Fronts propagating with curvature-dependent speed: Algorithms based on Hamilton-Jacobi formulations," *Journal of Computational Physics*, vol. 79, no. 1, pp. 12–49, 1988.

[72] S. R. Williams and A. P. Philipse, "Random packings of spheres and spherocylinders simulated by mechanical contraction," *Physical Review E*, vol. 67, no. 5, p. 051301, 2003.

[73] S. Torquato and Y. Jiao, "Robust algorithm to generate a diverse class of dense disordered and ordered sphere packings via linear programming," *Physical Review E—Statistical, Nonlinear, and Soft Matter Physics*, vol. 82, no. 6, p. 061302, 2010.

[74] M. Schneider, "The sequential addition and migration method to generate representative volume elements for the homogenization of short fiber reinforced plastics," *Computational Mechanics*, vol. 59, no. 2, pp. 247–263, 2017.

[75] M. Schneider, "An algorithm for generating microstructures of fiber-reinforced composites with long fibers," *International Journal for Numerical Methods in Engineering*, vol. 123, no. 24, pp. 6197–6219, 2022.

[76] X. Garcia, J.-P. Latham, J.-s. XIANG, and J. Harrison, "A clustered overlapping sphere algorithm to represent real particles in discrete element modelling," *Geotechnique*, vol. 59, no. 9, pp. 779–784, 2009.

[77] B. Sonon, B. François, and T. Massart, "A unified level set based methodology for fast generation of complex microstructural multi-phase RVEs," *Computer methods in applied mechanics and engineering*, vol. 223, pp. 103–122, 2012.

[78] M. Schneider, T. Hofmann, H. Andrä, P. Lechner, F. Ettemeyer, W. Volk, and H. Steeb, “Modelling the microstructure and computing effective elastic properties of sand core materials,” *International Journal of Solids and Structures*, vol. 143, pp. 1–17, 2018.

[79] B. Sonon, B. François, and T. Massart, “An advanced approach for the generation of complex cellular material representative volume elements using distance fields and level sets,” *Computational mechanics*, vol. 56, no. 2, pp. 221–242, 2015.

[80] B. Sonon and T. J. Massart, “A level-set based representative volume element generator and XFEM simulations for textile and 3D-reinforced composites,” *Materials*, vol. 6, no. 12, pp. 5568–5592, 2013.

[81] S. Karki, M.-C. Hsu, A. Krishnamurthy, and B. Ganapathysubramanian, “Mechanics Simulation with Implicit Neural Representations of Complex Geometries,” *arXiv preprint arXiv:2507.03087*, 2025.

[82] W.-D. Lian, G. Legrain, and P. Cartraud, “Image-based computational homogenization and localization: comparison between X-FEM/levelset and voxel-based approaches,” *Computational Mechanics*, vol. 51, no. 3, pp. 279–293, 2013.

[83] T.-P. Fries, “A corrected XFEM approximation without problems in blending elements,” *International Journal for Numerical Methods in Engineering*, vol. 75, no. 5, pp. 503–532, 2008.

[84] É. Béchet, H. Minnebo, N. Moës, and B. Burgardt, “Improved implementation and robustness study of the X-FEM for stress analysis around cracks,” *International journal for numerical methods in engineering*, vol. 64, no. 8, pp. 1033–1056, 2005.

[85] A. Menk and S. P. Bordas, “A robust preconditioning technique for the extended finite element method,” *International Journal for Numerical Methods in Engineering*, vol. 85, no. 13, pp. 1609–1632, 2011.

[86] L. Berger-Vergiat, H. Waisman, B. Hiriyur, R. Tuminaro, and D. Keyes, “Inexact Schwarz-algebraic multigrid preconditioners for crack problems modeled by extended finite element methods,” *International Journal for Numerical Methods in Engineering*, vol. 90, no. 3, pp. 311–328, 2012.

[87] H. Waisman and L. Berger-Vergiat, “An adaptive domain decomposition preconditioner for crack propagation problems modeled by XFEM,” *International Journal for Multiscale Computational Engineering*, vol. 11, no. 6, 2013.

[88] K. Kergrene, I. Babuška, and U. Banerjee, “Stable generalized finite element method and associated iterative schemes; application to interface problems,” *Computer Methods in Applied Mechanics and Engineering*, vol. 305, pp. 1–36, 2016.

[89] C. Lehrenfeld and A. Reusken, “Optimal preconditioners for Nitsche-XFEM discretizations of interface problems,” *Numerische Mathematik*, vol. 135, pp. 313–332, 2017.

[90] I. Babuška and U. Banerjee, “Stable generalized finite element method (SGFEM),” *Computer Methods in Applied Mechanics and Engineering*, vol. 201, pp. 91–111, 2012.

[91] P. Zhu and Q. Zhang, “BDF Schemes in stable generalized finite element methods for parabolic interface problems with moving interfaces,” *Computer Modeling in Engineering & Sciences*, vol. 124, no. 1, pp. 107–127, 2020.

[92] W. Gong and Q. Zhang, “Multi-grid methods of stable generalized finite element methods for interface problems,” *Engineering Analysis with Boundary Elements*, vol. 166, p. 105860, 2024.

[93] F. Gehrig and M. Schneider, “Improved Numerical Robustness of the X-FFT Solver via Internal Scaling,” *PAMM*, vol. 25, no. 4, p. e70042, 2025.

[94] M. Schneider, “Voxel-based finite elements with hourglass control in FFT-based computational homogenization,” *International Journal for Numerical Methods in Engineering*, vol. 123, no. 24, pp. 6286–6313, 2022.

[95] I. A. Sadarjoen, A. J. de Boer, F. H. Post, and A. E. Mynett, “Particle tracing in σ -transformed grids using tetrahedral 6-decomposition,” in *Visualization in Scientific Computing'98: Proceedings of the Eurographics Workshop in Blaubeuren, Germany April 20–22, 1998*, pp. 71–80, Springer, 1998.

[96] M. Schweiger and S. Arridge, “Basis mapping methods for forward and inverse problems,” *International journal for numerical methods in engineering*, vol. 109, no. 1, pp. 3–28, 2017.

[97] L. Shunn and F. Ham, “Symmetric quadrature rules for tetrahedra based on a cubic close-packed lattice arrangement,” *Journal of Computational and Applied Mathematics*, vol. 236, no. 17, pp. 4348–4364, 2012.

[98] M. Schneider, “A dynamical view of nonlinear conjugate gradient methods with applications to FFT-based computational micromechanics,” *Computational Mechanics*, vol. 66, no. 1, pp. 239–257, 2020.

[99] D. Merkert, H. Andrä, M. Kabel, M. Schneider, and B. Simeon, *An efficient algorithm to include sub-voxel data in FFT-based homogenization for heat conductivity*, pp. 267–279. Springer, 2015.

- [100] M. Schneider, “Superaccurate effective elastic moduli via postprocessing in computational homogenization,” *International Journal for Numerical Methods in Engineering*, vol. 123, no. 17, pp. 4119–4135, 2022.
- [101] Z. Hashin *et al.*, *The elastic moduli of heterogeneous materials*, vol. 9. US Department of Commerce, Office of Technical Services Washington, DC, 1960.
- [102] M. Schneider, F. Ospald, and M. Kabel, “Computational homogenization of elasticity on a staggered grid,” *International Journal for Numerical Methods in Engineering*, vol. 105, no. 9, pp. 693–720, 2016.
- [103] E. Donval, M. Schneider, H. Grimm-Strele, M. Godehardt, R. Burger, P. Lechner, D. Günther, and H. Andrä, “A directional contraction method to model sand-based binder jet 3D printed materials,” *International Journal of Solids and Structures*, vol. 312, p. 113260, 2025.
- [104] Y. Lin, Z.-Y. Yin, X. Wang, and L. Huang, “A systematic 3D simulation method for geomaterials with block inclusions from image recognition to fracturing modelling,” *Theoretical and Applied Fracture Mechanics*, vol. 117, p. 103194, 2022.
- [105] C. Lauff, M. Schneider, J. Montesano, and T. Böhlke, “Generating microstructures of long fiber reinforced composites by the fused sequential addition and migration method,” *International Journal for Numerical Methods in Engineering*, vol. 125, no. 22, p. e7573, 2024.
- [106] C. Lauff, M. Schneider, and T. Böhlke, “Microstructure generation of long fiber reinforced hybrid composites using the fused sequential addition and migration method,” *Journal of Thermoplastic Composite Materials*, pp. 2855–2893, 2025.
- [107] D. C. Company, “C711–70RNA polypropylene resin,” 2003.
- [108] P. F. Glass, “TufRov® 4575,” *Data Sheet*, 2013.
- [109] M. Kästner, G. Haasemann, and V. Ulbricht, “Multiscale XFEM-modelling and simulation of the inelastic material behaviour of textile-reinforced polymers,” *International Journal for Numerical Methods in Engineering*, vol. 86, no. 4-5, pp. 477–498, 2011.
- [110] F. Gehrig and M. Schneider, “Element-based internal variable formulations for finite element discretizations in FFT-based homogenization methods,” *International Journal for Numerical Methods in Engineering*, vol. 126, no. 21, p. e70170, 2025.